nature chemical biology

ARTICLES

https://doi.org/10.1038/s41589-021-00919-y

Check for updates

A counter-enzyme complex regulates glutamate metabolism in *Bacillus subtilis*

Vijay Jayaraman[1]✉, D. John Lee[2,4], Nadav Elad[3,4], Shay Vimer[1], Michal Sharon[1], James S. Fraser[2]✉ and Dan S. Tawfik[1,5]

Multi-enzyme assemblies composed of metabolic enzymes catalyzing sequential reactions are being increasingly studied. Here, we report the discovery of a 1.6 megadalton multi-enzyme complex from *Bacillus subtilis* composed of two enzymes catalyzing opposite ('counter-enzymes') rather than sequential reactions: glutamate synthase (GltAB) and glutamate dehydrogenase (GudB), which make and break glutamate, respectively. In vivo and in vitro studies show that the primary role of complex formation is to inhibit the activity of GudB. Using cryo-electron microscopy, we elucidated the structure of the complex and the molecular basis of inhibition of GudB by GltAB. The complex exhibits unusual oscillatory progress curves and is necessary for both planktonic growth, in glutamate-limiting conditions, and for biofilm growth, in glutamate-rich media. The regulation of a key metabolic enzyme by complexing with its counter enzyme may thus enable cell growth under fluctuating glutamate concentrations.

Metabolites are key cellular resources and their homeostasis is primarily achieved by regulating enzyme activities at various levels: transcription, translation and post-translation. While regulation of transcription and translation prevents the waste of resources and generally enables near-complete silencing of enzyme activity, post-translational enzyme regulation—including allosteric regulation via small molecules, covalent modification and degradation—enables rapid changes in metabolite levels. Regulatory modes at these various levels are crucial for the fitness of the organism[1–3]. Besides these modes of regulation, evidence is accumulating of transient enzyme complexes, or metabolons (typically composed of enzymes catalyzing sequential reactions)[4] that increase the metabolic efficiency by compartmentalization of reaction intermediates[5,6]. In this study, we describe a distinct mode of regulation where two central metabolic enzymes that catalyze opposite reactions ('counter enzymes') form a transient complex under metabolite-limiting conditions.

Our study arose from the search for the regulatory mechanism of glutamate dehydrogenase, GudB, from *B. subtilis*. Glutamate dehydrogenases reside at the crossroads of carbon and nitrogen metabolism by catalyzing the interconversion of glutamate to α-ketoglutarate (AKG) and ammonia. Glutamate is a major nitrogen reservoir and can provide up to 85% of the cellular nitrogen requirement in bacteria[7]. Moreover, glutamate has multiple other roles, including intracellular pH buffering, maintenance of osmolarity and acting as a counter ion to potassium[8,9]. Glutamate (Glu) is also one of the most abundant metabolites with cellular concentrations up to 150 mM (refs. [10–12]). In contrast, AKG is maintained at low concentrations, in the range of a few millimolar, and has rapid turnover[13]. In most Bacilli species, the Glu/AKG balance is maintained by the activity of catabolic, nicotinamide adenine dinucleotide (NAD^+) -dependent, dehydrogenases that degrade glutamate, with GudB being the key player in *B. subtilis*[14]. The other enzyme that directly affects the Glu/AKG balance is glutamate synthase (GltAB), a heterodimeric enzyme composed of two subunits, GltA and GltB, which is involved in glutamate synthesis starting from glutamine and AKG (Fig. 1a). Notably, *B. subtilis* is known to rapidly adapt to loss or inactivation of genes involved in glutamate metabolism by suppressor mutations, suggesting the importance of glutamate homeostasis in this bacterium[15].It should be noted that, GudB is cryptified and inactive in the domesticated strain, *B. subtilis* 168 (ref. [16]), however, the wild-type strain NCIB 3610 used in this study, encodes a functional copy of GudB.

While not much is known about the posttranslational regulation of glutamate synthases (such as GltA/B), glutamate dehydrogenases (such as GudB) are among the most intricately regulated enzymes—they are renowned, if not infamous, for their complex allosteric regulatory features[17]. The mammalian glutamate dehydrogenases are regulated by nucleotides[18], while some bacterial enzymes are regulated by amino acids such as leucine[19]. The *B. subtilis* GudB is constitutively expressed[14,16], and at high levels, and hence regulation is critical. However, nucleotides, amino acids and other key metabolites we have tested in vitro have all failed to regulate GudB's activity[14].

Here we investigated the regulatory mode of GudB in *B. subtilis*. We found that under conditions where glutamate needs to be synthesized, GudB binds to its counter enzyme, GltAB. Growth profiling of relevant strains and steady-state kinetic measurement suggested that GudB is silenced on binding GltAB. The regulatory interplay of the enzymes in the complex results in a unique oscillatory progress curve. Native mass spectrometry (native MS), and high-resolution cryo-EM structures, revealed the molecular basis of GudB- inhibition in this unusually large (1.6 MDa) complex. Besides being crucial for planktonic growth in a glutamate-limiting condition, we also show that GudB–GltAB complex formation is needed for optimal biofilm development, even in a glutamate-rich medium. This counter-enzyme assembly may thus mediate the previously observed spatiotemporal glutamate catabolism in biofilms[20].

[1]Department of Biomolecular Sciences, Weizmann Institute of Science, Rehovot, Israel. [2]Department of Bioengineering and Therapeutic Sciences, University of California San Francisco, San Francisco, CA, USA. [3]Department of Chemical Research Support, Weizmann Institute of Science, Rehovot, Israel. [4]These authors contributed equally: D. John Lee, Nadav Elad. [5]Deceased: Dan S. Tawfik. ✉e-mail: vijay.jayaraman@weizmann.ac.il; jfraser@fraserlab.com

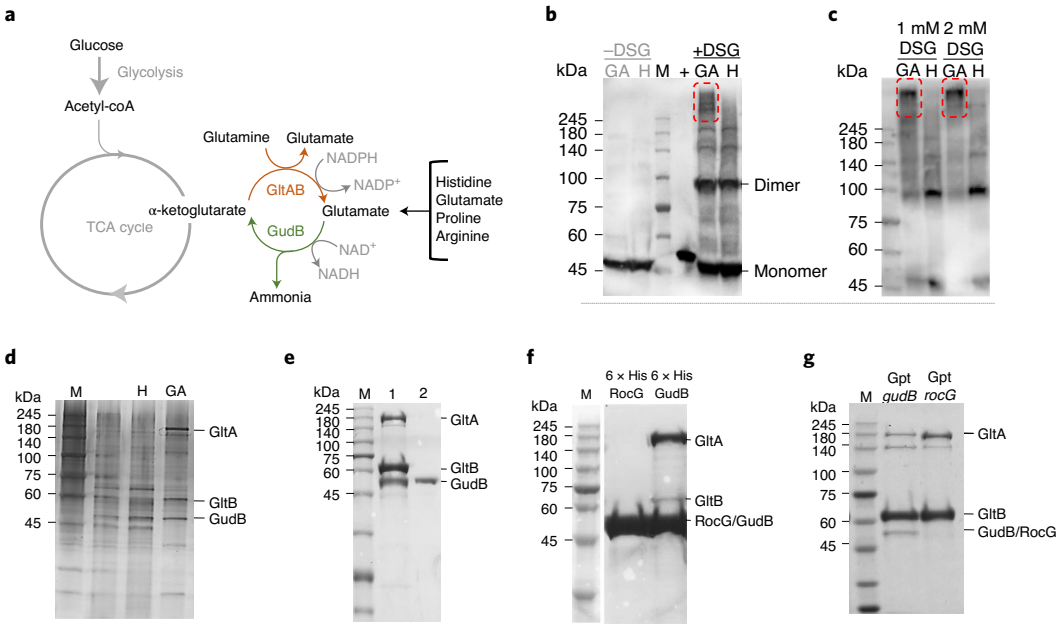

Fig. 1 | GudB interacts with GltAB in glutamate-poor growth conditions. a, Key reactions involved in glutamate metabolism in *B. subtilis*. Amino acids such as proline, arginine and histidine when provided as the sole C/N source are catabolized via glutamate. In contrast, growth on glucose as C source demands glutamate synthesis (via AKG). **b**, Western blot using anti-GudB antibodies indicating similar expression levels of GudB in *B. subtilis* cells grown in glucose ammonia (GA) and histidine (H) (−DSG). On treating with a chemical crosslinker (DSG, 0.5 mM), high molecular weight species that include GudB can be seen in cells grown on glucose ammonia (GA, highlighted in the dashed red frame) but not on histidine (H). Recombinant GudB served as a positive control (+). **c**, The high molecular weight species of GudB are clearly seen in western analysis of lysates from cells grown on glucose ammonia (as in C) yet treated with higher concentration of DSG (1 mM/2 mM). **d**, Immunoprecipitation of GudB indicated coelution of GltA and GltB in glucose ammonia but not in histidine. The eluates from the pulldown were subjected to SDS-PAGE and stained with silver nitrate. **e**, SDS-PAGE showing coelution of GudB and GltA on purification of Strep-GltB from *B. subtilis* cells grown in glucose ammonia (Lane 1; Lane 2 shows purified recombinant Strep tagged GudB). **f**, Copurification of GltA and GltB on pulldown of His-tagged GudB but RocG. **g**, GudB but not RocG coeluted on pulldown of Strep-GltB from strains expressing either GudB or RocG from the constitutive *gudB* promoter (Gpt). Images in **b**–**g** correspond to one replicate and are representative at least three independent experiments.

Results

GudB interacts with GltAB in glutamate-poor growth conditions. *B. subtilis* grows in both glucose-ammonia (glutamate-poor) and in histidine/glutamate (glutamate-rich) -containing medium. Besides histidine and glutamate, growth on proline or arginine results in glutamate-rich conditions, as these amino acids are catabolized via glutamate as an intermediate (Fig. 1a). Oddly, the protein levels of GudB are the same in cells grown in glucose-ammonia and in histidine (Fig. 1b, −DSG). We probed the oligomeric state of GudB in both conditions using in vivo crosslinking of cells using dissucinimidyl glutarate (DSG) followed by western blotting using anti-GudB antibodies (Fig. 1b, +DSG). In glucose-ammonia we observed bands with a molecular weight greater than hexameric GudB, the expected oligomeric state of the enzyme[21], while in histidine the bands indicated dissociated monomer/dimer species. This discrepancy is even greater in high crosslinker concentration (Fig. 1c). The high molecular weight species is specific to glutamate-poor media such as glucose-ammonia and was not seen in any of the glutamate-rich media (glutamate, histidine, arginine or glycerol-glutamate) we tested (Extended Data Fig. 1a).

Immunoprecipitation of GudB from cells grown in glucose ammonia showed two additional proteins along with GudB), with molecular weights around 160 and 60 kDa. This interaction was specific to cells grown in glucose-ammonia but not in histidine (Fig. 1d). Shotgun proteomics of the eluates indicated that these proteins are GltA (168.7 kDa) and GltB (54.8 kDa). Both proteins were notably enriched in eluates obtained from glucose ammonia-grown cells compared to histidine grown ones (≤167-fold with crosslinker and ≤21-fold without; Supplementary Table 1 and Supplementary Datasets 1 and 2). Expression and pulldown of TwinStrep-tagged GltB (GltB-TS) from cells grown on glucose ammonia also indicated the formation of a ternary GudB–GltAB complex (Fig. 1e). This association was surprising as GltAB, a heterodimeric glutamate synthase, is involved in glutamate synthesis, the opposing function to GudB. Unlike GudB, GltAB expression is highly regulated[22,23]. Indeed, GltAB is exclusively expressed in glutamate-poor conditions (Extended Data Fig. 1b). Thus, it is likely that in glutamate-rich conditions, the GudB–GltAB complex is absent simply because GltAB is not present.

The interaction with GltAB is paralog specific. GudB is not the only catabolic glutamate dehydrogenase in *B. subtilis*. Its closely related paralog, RocG, shares 75% sequence identity and an effectively identical hexameric structure[21]. Moreover, GudB and RocG share similar kinetic properties with respect to glutamate degradation[14]. RocG is a part of the Roc operon involved in arginine degradation and its transcription is tightly regulated. Accordingly, the levels of RocG in glucose ammonia is up to 30-fold lower compared to GudB. Both in vitro (Fig. 1f) and in vivo (Fig. 1g) pulldown experiments indicated that RocG does not interact with GltAB. Notably, this explains the severe growth defects of the strain constitutively expressing RocG (instead of GudB) in glucose-ammonia[14]. Given the lack of interaction of RocG with GltAB, strains consitutively expressing RocG can be used as a control to assess the regulation of GudB by GltAB.

GltAB negatively regulates GudB activity in vivo. Having established that GudB forms a complex with its counter-enzyme, GltAB,

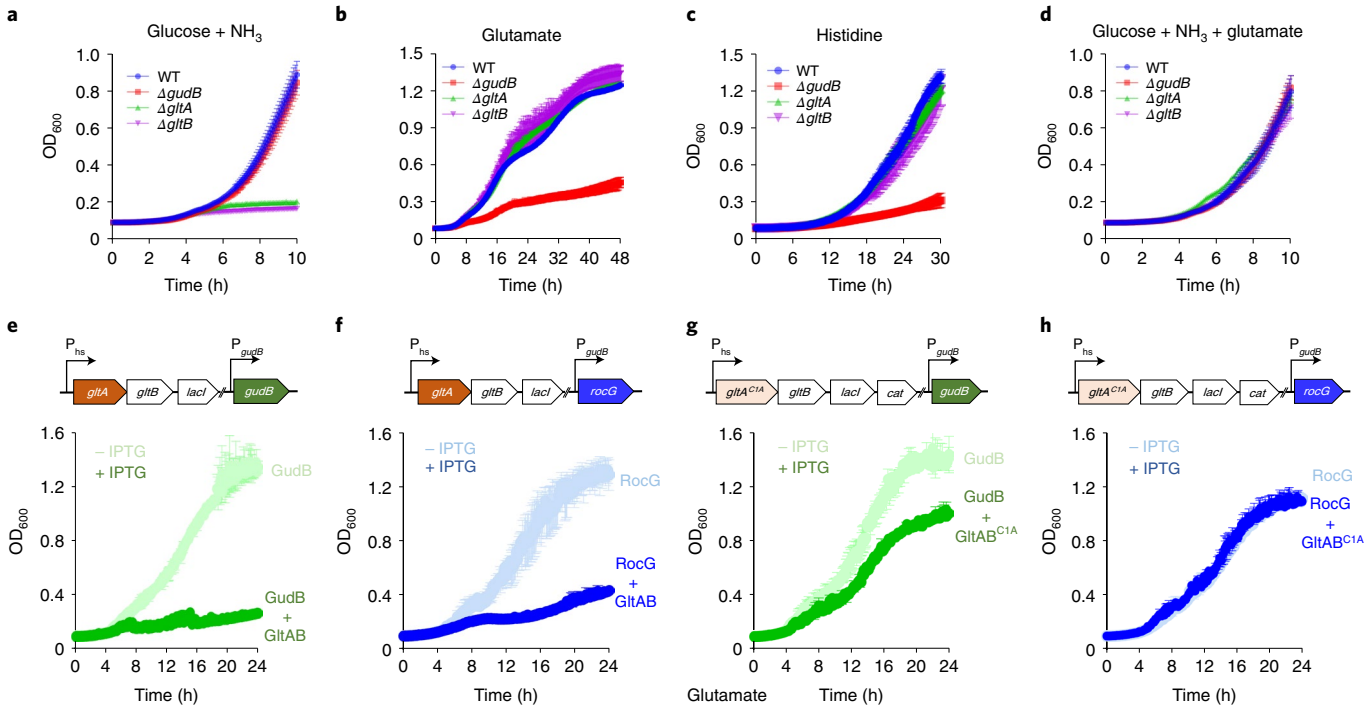

Fig. 2 | The phenotypic effects of GltAB and GudB and their interaction. a–d, Growth profiling of the denoted knockout strains indicate that GltAB's glutamate dehydrogenase activity is essential for growth in glucose-ammonia (**a**) while GudB's glutamate dehydrogenase activity is essential in glutamate (**b**) and histidine (**c**). Under conditions where both glucose and glutamate are available neither of these two activities is essential (**d**). $n=3$ are three independent measurements. Data are presented as mean of all measurements and error bars represent the s.d. **e–h**, Growth inhibition in glutamate medium on expression of wild-type GltAB, and its inactive mutant (GltA^{C1A}), from an IPTG-inducible hyperspank promoter. The scheme above each panel shows the genotype of the corresponding strain. Expression of functional GltA causes growth suppression in strains expressing GudB (**e**) or RocG (**f**) probably due to futile cycling of making and breaking glutamate. Expression of GltAB^{C1A} causes growth suppression in a strain expressing GudB (**g**) but not in a strain coexpressing RocG (**h**). These effects are in agreement with GltA interacting with and inhibiting GudB but not RocG $n=2$ are two independent measurements. Data are presented as mean of all measurements and error bars represent the s.d. WT, wild-type.

we next aimed to decipher the role of GudB–GltAB complex formation in vivo. We profiled the growth of individual knockout strains Δ*gudB*, Δ*gltA* and Δ*gltB* in media where either glutamate synthesis or catabolism should dominate. In general, we observed that when GltAB is essential, GudB is dispensable (Fig. 2a) and vice versa (Fig. 2b,c: note that removal of either of GltAB's subunits leads to complete loss of the synthase activity). Specifically, the catabolic GudB is essential when glutamate (Fig. 2b) or other amino acids, such as histidine (Fig. 2c) that are catabolized via glutamate, are present as the sole carbon source. Conversely, the anabolic GltAB is essential when glutamate needs to be synthesized de novo, as indicated by the inability of either Δ*gltA* or Δ*gltB* to grow on glucose ammonia (Fig. 2b). Finally, neither GudB nor GltA/B are required when glucose-ammonia is supplemented with glutamate (Fig. 2d).

Given the orthogonal functions, we surmised that GudB–GltAB complex formation could be inhibiting GudB's activity to avoid the futile cycle of glutamate synthesis and breakdown. If this is indeed the case, then the complex formation should be deleterious under conditions where glutamate is the sole carbon source and GudB's activity is pivotal. We observed that expression of GltAB in the background of a strain constitutively expressing GudB causes a severe growth defect (Fig. 2e). However, a similar phenotype was seen when GltAB is expressed in the strain constitutively expressing RocG (Fig. 2f), suggesting that growth inhibition in both the cases is mostly the result of futile cycling of making and breaking glutamate that will consume large amounts of nicotinamide adenine dinucleotide phosphate (NADPH) and ATP due to glutamine hydrolysis. To disentangle the role of futile cycling from GltAB–GudB complex association, we expressed a catalytically inactive mutant of GltAB^{C1A} (Extended Data Fig. 1c) alongside GudB, (Fig. 2g). Here, the growth inhibition probably results from the physical interaction bewteen GudBs and GltAB, as validated by pulldowns of the GudB–GltAB^{C1A} complex under the same growth condition (Extended Data Fig. 1d). Further, no growth inhibition was observed when the inactive GltAB^{C1A} was coexpressed with RocG (Fig. 2h; and accordingly, GltAB^{C1A} was pulled down on its own, Extended Data Fig. 1d). Inducible expression of GltAB was verified by the isopropyl-β-D-thiogalactoside- (IPTG-)dependent growth of the strains in glucose ammonia (Extended Data Fig. 2). Taken together, these results support a key regulatory role for the GudB–GltAB complex in silencing GudB under glutamate-poor conditions.

GltAB binding alters the kinetic properties of GudB. To understand the effects of complex formation on the activity of the component enzymes, the complex, and the individual enzymes, were purified from *B. subtilis* (Fig. 3a) and used for steady-state kinetic measurements. The complex exhibited either glutamate synthase or dehydrogenase activity depending on which substrates were added (Fig. 3b), and the steady-state kinetic parameters were accordingly derived from initial velocity measurements (Supplementary Table 2 and Extended Data Fig. 3a–f). The activity of GltAB is essentially the same on its own and in complex with GudB (a moderate increase in catalytic efficiency was observed when in complex with GudB). However, GudB showed altered behavior: the K_M value

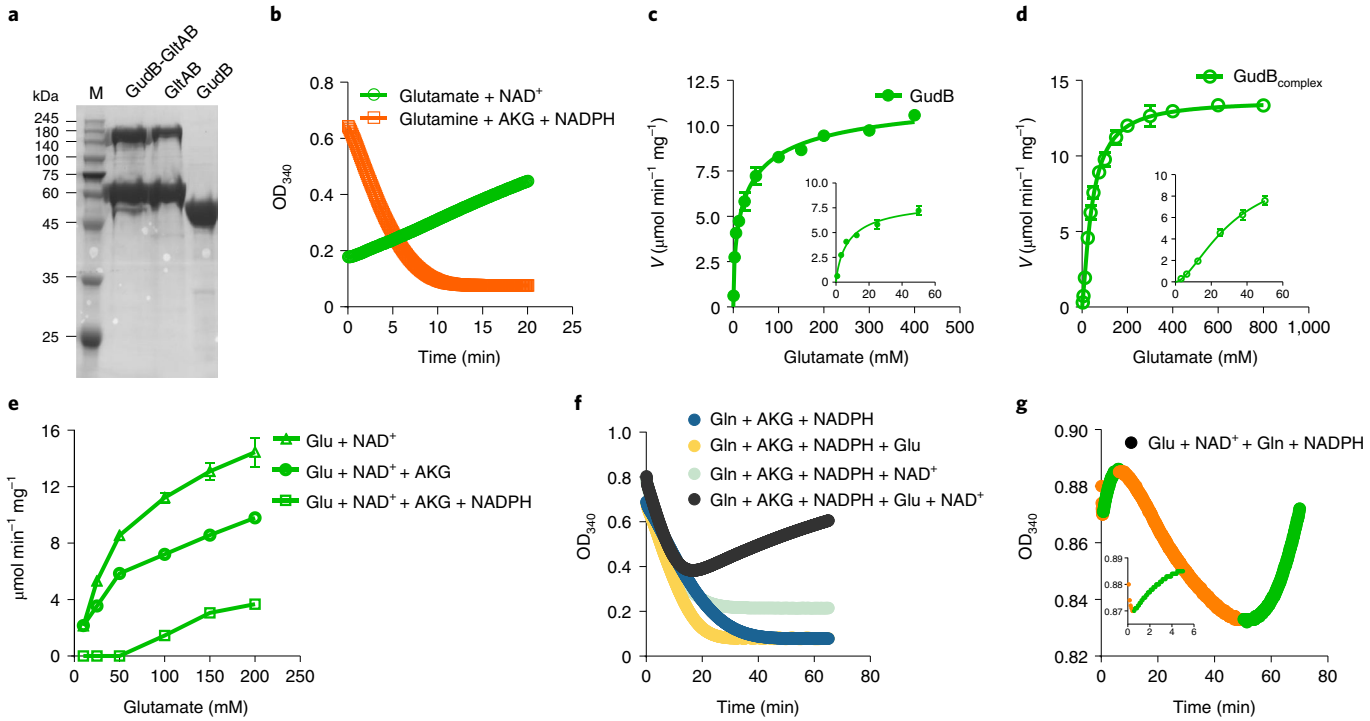

Fig. 3 | Enzymatic kinetics of the GltAB–GudB complex. a, SDS–PAGE analysis of the GltAB–GudB complex, and its individual components, GudB and GltAB, used in these assays. The complex and standalone GltAB were purified by the pulldown of Strep-GltB from respective *B. subtilis* strains (Methods). GudB was purified by recombinant expression in *E. coli*. **b**, The GudB–GltAB complex exhibits either glutamate dehydrogenase activity (on addition of glutamate and NAD^+; green line, indicating a drop in absorbance at 340 nm due to NAD^+ reduction) or synthetase activity (on addition of AKG, glutamine and NADPH; the orange line indicating an increase in absorbance due to NADPH oxidation). **c**,**d**, Initial velocity of the dehydrogenase reaction as a function of glutamate concentration. **c**, On its own, GudB displayed a K_M value of 7.3 mM for glutamate and negative cooperativity (Hill coefficient of 0.57, Supplementary Table 2). **d**, In complex with GltAB, the K_M rises to 138 mM with positive cooperativity ($H = 1.3$). The insets in **c** and **d** show the initial velocities at low concentrations of glutamate. $n = 2$ are two independent experiments. Data are presented as mean and error bars indicate standard deviation. **e**, Initial velocity of the dehydrogenase reaction in the GltAB–GudB complex, as is (Glu + NAD^+), and in the presence of GltAB's substrates (AKG, NADPH). $n = 2$ are two independent experiments. Data are presented as mean and error bars indicate standard deviation. **f**, Reaction progress curves of the GudB–GltAB complex with various substrate combinations: substrates of GltAB only (blue), substrates of GltAB plus glutamate (yellow), substrates of GltAB plus NAD^+ (light blue), all substrates for both enzymes (black). **g**, Multiphasic progress curve displayed by the GudB–GltAB complex in the presence of substrates of both enzymes except AKG. The phases where GltAB predominates are shown in orange and those where GudB is dominant are shown in green. The inset shows the initial few minutes of the reaction where there is a rapid drop in absorbance followed by a gradual increase. **a**,**b**,**f** and **g** correspond to one experiment and are representative of at least four independent experiments.

for glutamate is roughly 19 times higher in the complex (7.3 mM for free GudB, Fig. 3c, versus 138 mM for the GltAB bound form, Fig. 3d), supporting the notion that GltAB binding suppresses GudB's activity. While the above measurements allowed us to derive kinetic parameters, the assay conditions do not reflect the cellular scenario where the substrates of both enzymes are present. Indeed, addition of GltAB's substrates, AKG and NADPH, completely inactivates GudB at glutamate concentrations up to 50 mM (Fig. 3e). The silencing effect requires both substrates as neither AKG nor NADPH exhibited a substantial effect on their own. Using mass photometry, we observed that AKG and NADPH promote the assembly of GltA and GltB (Extended Data Fig. 3g). Moreover, we did identify AKG among other metabolites (Supplementary Table 3) extracted from the GudB–GltAB complex purified directly from *B. subtilis*. Overall, these results validate the hypothesis that GltAB's binding allosterically silences GudB's activity.

GltAB's regulatory role was further manifested when its third substrate, glutamine, was added, unexpectedly resulting in multiphasic progress curves. We monitor GltAB's activity through a decrease in absorbance (OD) at 340 nm (due to the reduction in NADPH levels) and GudB's activity through an increase in absorbance due to increase in NADH formation (Fig. 3b). In principle, if both enzymes are active, a steady state would be established with a monotonic progress curve, with positive or negative slope values depending on the relative catalytic efficiency of the two enzymes[24]. Contrary to this expectation, in the presence of saturating concentration of substrates of both enzymes, the GudB–GltAB complex displayed a biphasic progress curve (Fig. 3f). The slope of the first phase was identical to the one observed when GltAB activity was tested separately, suggesting that in this initial phase GudB is completely inactive due to the presence of AKG and NADPH (as shown in Fig. 3e). With the drop in NADPH concentration, GudB becomes active and this results in the onset of second phase of increasing absorbance. Indeed, when the reaction is initiated with all substrates except AKG, multiple oscillation cycles could be observed until most of the NADPH is consumed by GltAB, resulting in a final phase where GudB activity dominates (Fig. 3g and Extended Data Fig. 3h–l). Moreover, the oscillation frequency depends nonlinearly on the concentration of the complex (Extended Data Fig. 3m–o). These types of oscillation in enzyme reactions are unusual even when the assay mix contains two enzymes with opposing functions.

Structure of the GudB–GltAB complex. Native MS of the individual proteins provided preliminary information about the stoichiometry

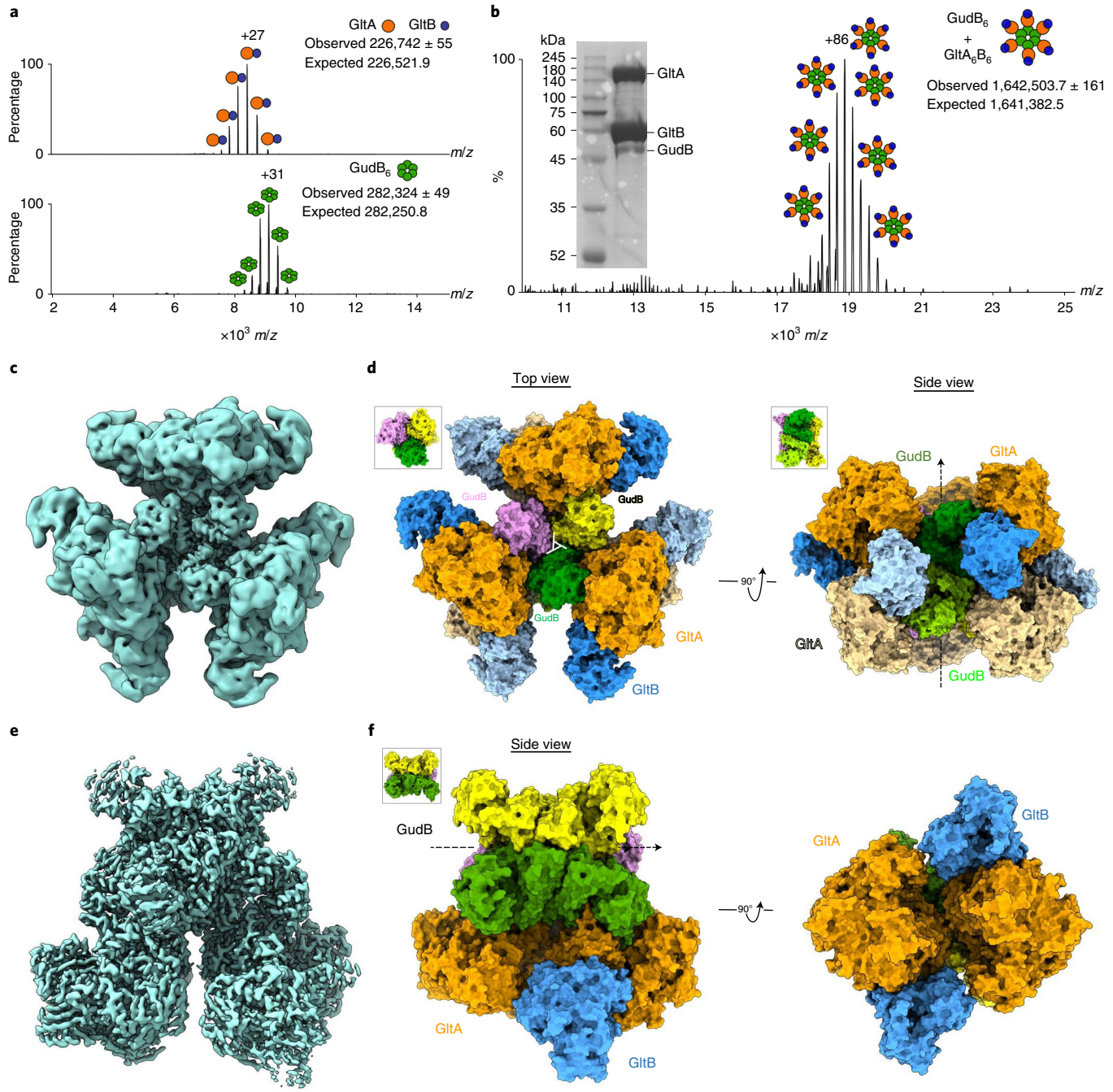

Fig. 4 | The stoichiometry, oligomeric state and atomic structure of the GltAB–GudB complex. a, Native MS of standalone GltAB (top) and GudB (bottom). The oligomeric state as inferred from the mass is shown schematically besides each charge state: GltAB's observed mass corresponds to a heterodimer, while GudB's mass indicated the expected hexamer. **b**, Native MS of the GudB–GltAB complex. The observed mass corresponds to six copies of a GltAB heterodimer bound to the GudB hexamer. The low *m/z* region contained unbound GltAB. **a**, The inset shows the SDS–PAGE of the protein sample used for native MS and cryo-EM. The image is from one batch of purification and is representative of at least four independent purifications. **c**, Density map of the $GudB_6$–$GltAB_6$ complex generated after applying D3 symmetry. **d**, Model of the $GudB_6$–$GltA_6B_6$ complex. The three dimers of the GudB hexamer are shown in three different colors (pink, yellow and green). GltA and GltB are shown in orange and blue, respectively. GltA and GltB subunits below the plane of the paper is shown in light orange and light blue, respectively. The views (top and side) are with respect to the orientation of GudB as shown in the insets. The dihedral (D_3) rotation axis of GudB is depicted as a triangle in the left panel and as a dashed arrow in the right panel. **e**, The density map of $GudB_6$–$GltA_2B_2$. **f**, On the left is shown the model of $GudB_6$–$GltA_2B_2$ (side view) and the right panel shows the model rotated 90° along the dihedral axis of GudB. From the model on the right, it is clear that there are minimal interactions between the two GltA copies.

of the individual enzymes. As observed previously[14,21], GudB forms a hexamer (Fig. 4a). However, unlike its closest homolog with a known structure, Azospirillum GltAB, which is predominantly a hetero-dodecamer[25,26], *B. subtilis* GltAB is a heterodimer (Fig. 4a). GltAB's oligomeric state therefore resembles that of ferredoxin-dependent glutamate synthases found in photosynthetic organisms such as plants or cyanobacteria[27,28]. The native MS of the GudB–GltAB complex (Fig. 4b) indicated a species with

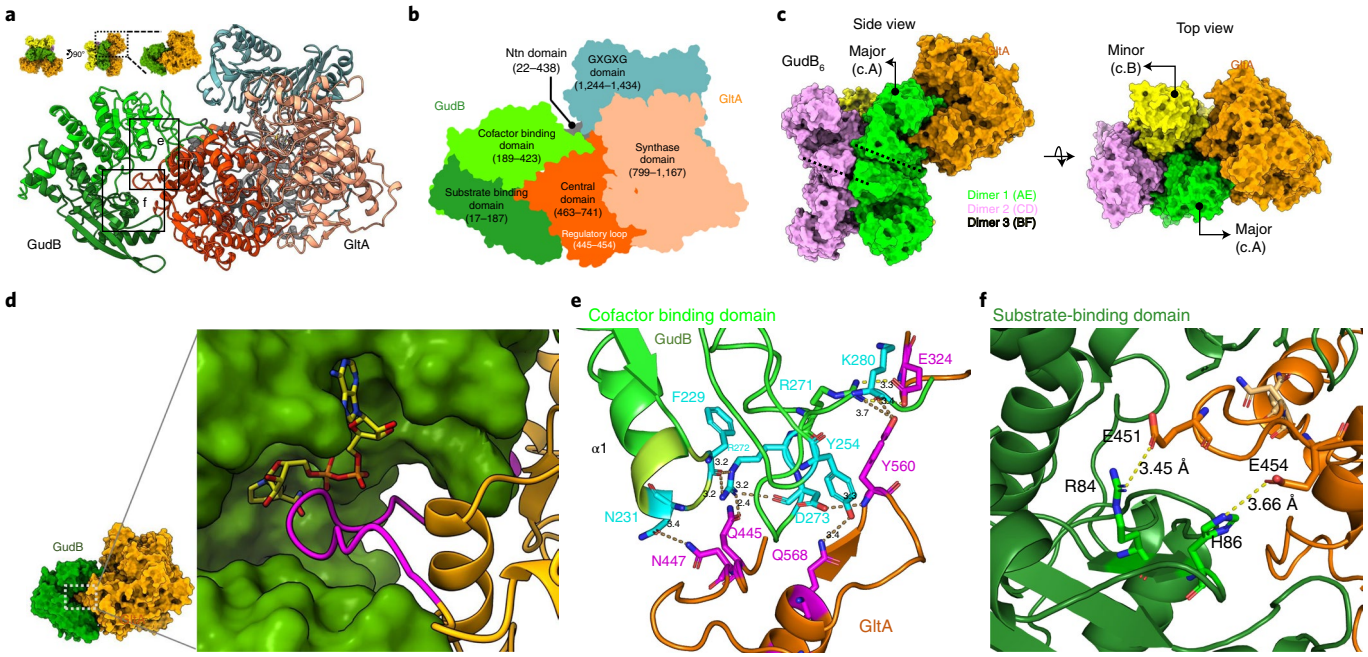

Fig. 5 | The structural basis for inhibition of GudB by GltA binding. a, Zoom-in model of the GudB-GltA interaction. The colors represent the different domains of GltA and GudB as detailed in the next panel. The inset shows the perspective of the model with respect to the model shown in Fig. 4f. The dashed boxes (**e** and **f**) correspond to the region containing residues from GudB and GltA forming a hydrogen bonding network. This is shown in detail in **e** and **f**. **b**, GltA consists of Ntn-amidotransferase (Ntn) domain (gray), a central domain (orange), a synthase domain (sand) and a GXGXG domain (metal blue). The central domain of GltA (orange) interacts with residues from both the substrate (green) and cofactor binding domain of GudB (light green). **c**, GudB's hexamer comprises a trimer of dimer; GltA (in orange) interacts with two protomers of GudB (major and minor) from two different dimers (green and yellow, respectively). The front view shows the major interacting GudB protamer, and the top view the minor one. The coloring pattern of the three dimers and the corresponding chain IDs are also shown. The dimer interface in two of the dimers (1 and 2) is shown as dashed lines. **d**, Zoom-in on GudB active-site cleft (surface display, in green) and the interacting loop of GltA (magenta; the remaining structure of GltA is in orange). NAD^+ (in yellow sticks) is modeled into the active-site cleft of GudB based on superposition of GltA-bound GudB to 1V9L (open state). The steric overlap of GltA's loop with NAD^+ would be even higher in the closed state of the enzyme. **e**, Zoom-in on the boxed region shown in **a**, depicting the hydrogen bonding network between residues of GltA (magenta) and the cofactor binding domain of GudB (cyan). Notably, GudB's N231, which is located at the tip of the phosphate binding loop (and binds the NAD^+'s phosphate groups) is bound to GltA's N447, and thus directly interferes with NAD^+ binding. **f**, The interaction of GltA's E451 and E454 with residues of the substrate-binding domain of GudB (R84 and H86).

a mass of roughly 1.6 MDa in the high *m/z* region, corresponding to six GudB protomers and six GltAB heterodimers ($GudB_6$–$GltA_6B_6$).

This GudB–GltAB complex is unusually large—almost half the size of the ribosome—and we set out to determine the structure of the complex using Cryo-EM. We were able to obtain the structure of the fully assembled complex at an overall resolution of 3.9 Å with D3 symmetry (Fig. 4c, Extended Data Fig. 4 and Supplementary Table 5). The structure unambiguously revealed that the complex comprises a GudB hexamer and six GltAB heterodimers (Fig. 4d). Each GltAB heterodimer makes contact with two protomers of GudB, with the interaction occurring solely through GltA. There are also no interactions between the GltAB heterodimers in the complex. Although the resolution of the map permitted assignment of the different chains, to reveal the mechanistic basis of GudB silencing by GltA, a map with higher resolution was needed.

Towards this, we increased the particle density, by addition of excess recombinant GudB to *B. subtilis* cell lysate before purifying the GudB–GltAB complex (inset in Extended Data Fig. 5a). Preliminary cryo-EM single particle analysis resulted in four three-dimensional (3D) classes representing a varied number (2–4) of GltAB heterodimers bound to the GudB hexamer (Extended Data Fig. 5b) in accordance with native MS showing a range of GudB–GltAB complexes (Extended Data Fig. 5a). The four resulting maps resemble the native complex ($GudB_6$-$GltA_6B_6$) but with varying occupancy of the GltAB heterodimers. The most abundant class corresponded to a GudB hexamer with two GltAB heterodimers ($GudB_6$–$GltA_2B_2$). A high-resolution map was prepared by collapsing these classes into a single class and refining with the preliminary $GudB_6$–$GltA_2B_2$ map as the initial reference. This refined to high-resolution (2.4 Å) with C2 symmetry (Fig. 4e,f, Extended Data Fig. 6 and Supplementary Table 5). The higher resolution model allowed us to determine the precise contacts used to stabilize GudB in an inactive state (Fig. 4f). There appear to be no substantial architectural differences on GltAB with the components of the structure of the hexameric GltAB from *Azospirillum brasiliense* (Protein Data Bank (PDB) ID 6s6x)[26], but the dimerization of GltA, which is a likely prerequisite for hexamer formation, is not observed. Among other contacts, the GltA homo-dimer interface includes 13 putative hydrogen bonds. Examination of the corresponding residues in *B. subtilis* GltA suggested that ten out of these 13 hydrogen bonds cannot be formed, which is in agreement with *B. subtilis* GltA not forming homo-dimers. The higher resolution did permit unambiguous assignment of two 4Fe–4S clusters in GltB, and 3Fe–4S clusters and the co-factor flavin mononucleotide (FMN) in GltA. These cofactors play a key role is shuttling electrons from the GltB-bound NADPH to 2-iminoglutarate that is formed in the synthase domain of GltA (Extended Data Fig. 7a), thus allowing the reduction of the latter to yield glutamate.

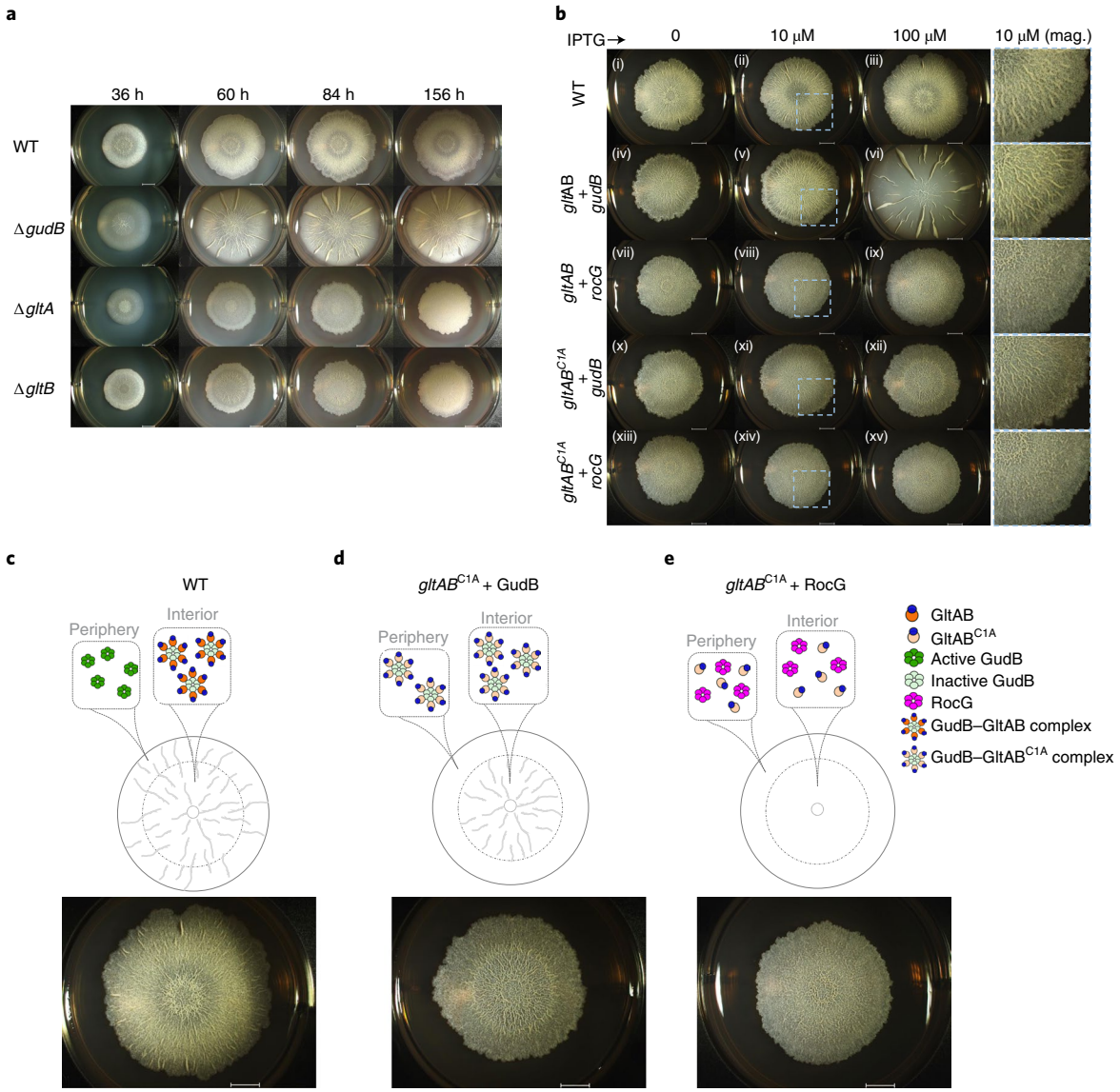

Fig. 6 | GudB–GltAB interaction is important for biofilm formation. a, Representative images of biofilms of wild-type and mutant *B. subtilis* strains on MSGG agar medium, monitored over a period of roughly 7 days. As indicated by their knockouts, both Glt subunits (GltA and B), and GudB, are essential for wild-type-like biofilm morphology **b**, Comparision of biofilm formation by wild-type and mutants expressing GltA under an IPTG-induced promoter, at varying IPTG concentrations (0–100 μM). Wild-type (i–iii); IPTG-induced GltA plus GudB (iv–vi), or RocG (vii–ix); IPTG-induced inactive GltA mutant, GltAB^{C1A} plus GudB (x–xii), or with RocG (xiii–xv). Wild-type GltAB and the GltAB^{C1A} were expressed from an IPTG-inducible hyperspank promoter, while GudB and RocG were under *gudB*'s promoter. Wild-type's biofilms are not affected by the presence of IPTG (i–iii). The strain expressing GltAB from an IPTG-induced promoter forms altered biofilms with no IPTG (iv), wild-type-like biofilms with low concentration of IPTG (v), while overexpression resulted in biofilms similar to those of the Δ*gudB* strain (vi). Coexpression of RocG and GltAB resulted in biofilms with no wrinkles (vii–ix). Expression of the inactive GltAB^{C1A} with GudB restores the morphology of the biofilm's interior, in an IPTG-dependent manner (x–xii); in contrast, coexpression of GltAB^{C1A} with RocG does not (xiii–xv). The scale bars in all images correspond to 4 mm. Magnified sections are shown in the last column of **b**. **c**–**e**, A summary of the biofilm disruption phenotypes and a proposed model that accounts for them (text). The biofilm images correspond to the following images from **b**: iii (**c**), xii (**d**) and xv (**e**).

The structural basis of GudB's inhibition by GltAB. GudB interacts with GltAB extensively through the GltA subunit (Fig. 5a) with few contacts between adjacent GltAB heterodimers (Fig. 4f, right panel). GltA is a multi-domain protein that consists of an Ntn-amidotransferase domain, a central domain, a synthase domain and the GXGXG domain (Fig. 5b). The interactions with GudB occur primarily with GltA's central domain that docks onto the active-site cleft of GudB, which separates GudB's cofactor (NAD^+) and substrate (glutamate) binding domains (Fig. 5a). The relative movement of these two domains results in 'open' and 'closed' conformations that are a key part of the catalytic cycle of glutamate dehydrogenases[29]. Cleft closure brings NAD^+ close to glutamate thereby enabling the hydride transfer, as represented by the substrate bound structure of glutamate dehydrogenase from *Aspergillus niger* (PDB 5XVX)[30]. Based on the distance between residues R280 and K122 as a proxy of the degree of closeness, GltA-bound GudB is in the open state ($d = 29.1$ Å, Extended Data Fig. 7b).

Another key observation is that each GltA subunit interacts with two adjacent GudB subunits (Fig. 5c), which provides a molecular

explanation for how GltA binding stabilizes the GudB hexamer (Extended Data Fig. 7c). The primary interacting subunit ('major') of GudB, with an intersubunit contact area of GudB:GltA of 1,931:1,817 (Å^2), has its active site blocked as described above. The neighboring subunit ('minor') interacts with a much smaller surface area (360 Å^2), outside the active site (Fig. 5c, top view). However, the paralog specificity of GltA for GudB is likely explained by the lack of conservation in RocG for residues mediating this secondary 'minor' interaction (underlined in Extended Data Fig. 8a and Supplementary Table 4) in addition to steric clashes by RocG specific residues such as M277 instead of T277 in GudB The key 'major' interactions between GudB and GltA involve a long loop, 'the GudB regulatory loop' that connects the Ntn and central domains of GltA (residues 445–455). This loop extends across the active-site cleft of GudB. Residues from the loop interact with both the cofactor- and substrate-binding domains of GudB (Fig. 5d–f). Foremost, a network of hydrogen bonds is observed between GltA residues and the cofactor binding domain of GudB (Fig. 5e), which in turn stabilizes multiple loops in GudB. Notably, clear density for these loops is seen in the complex but not in the apo-GudB crystal structure[21] or in the GudB subunits in the complex that are not bound to GltA. The ordering of the cofactor binding domain of GudB by binding to GltA is also reflected in the lower average B-factor of the GltA-bound GudB compared to the unbound (Extended Data Fig. 8b). The most notable contact is between the tip of α1 and residue N231 of GudB's NAD^+ binding domain, which is typically used by Rossman folds to bind the diphosphate group of NAD^+. Consequently, GltA binding precludes NAD^+ binding to GudB. Moreover, as shown in Fig. 5e, GltA's regulatory loop occupies a specific position in the active-site cleft of GudB that is otherwise occupied by the cofactor in the closed (and catalytically active) conformation of the enzyme. Thus, stabilization of the open conformer, and blocking NAD^+ binding by steric hindrance are both probably key to GudB inhibition by GltAB. While mass spectrometry studies identified several ligands retained by the complex (Supplementary Table 3), the cryo-EM experiments did not reveal any density consistent with AKG or NADPH in the active site. AKG and NADPH dependence on complete inhibition of GudB could be due to long distance allosteric effect of the binding of these ligands. The relative location of AKG binding site in GltA and NADPH binding site in GltB, with respect to the regulatory loop that interacts with GudB active-site cleft is shown in Extended Data Fig. 8c.

GudB–GltAB complex formation is key for the biofilm morphology. *Bacillus* forms biofilms in its natural environment, and glutamate metabolism plays a key role in their development[31–33]. Accordingly, in the laboratory, *B. subtilis* biofilms are usually grown in glutamate-rich media containing glycerol as the carbon source (MSGG). However, unlike planktonic growth, biofilm growth on solid agar presents spatiotemporal constraints: cells in the interior depend on the peripheral cells for glutamine, while the peripheral cells depend on the interior cells for ammonia[20]. Thus, the regulation of the GudB–GltAB complex could be central to this division of labor.

We initially examined the morphology of biofilms that are devoid of GudB, GltA or GltB. Unlike for planktonic growth (Fig. 2a–d), for wild-type like biofilm growth and morphology, all three proteins seem to be important (Fig. 6a). Δ*gudB* produced rapidly growing biofilms (Extended Data Fig. 9a) with large 'channels' running from the periphery to the interior. The Δ*gltA* and Δ*gltB* strains also showed biofilm morphologies that differ from wild-type: while the Δ*gltB* strain had wrinkles restricted to interior, the Δ*gltA* biofilm did not have any wrinkles. Since the enzymatic function, glutamate synthesis, is lost in the absence of either GltA or GltB, the different phenotypes are in agreement with the additional role for GltA in regulating GudB.

Next, we examined the role of GudB–GltAB complex formation on biofilm morphology. GltAB expression even at low levels (10 μM IPTG) was sufficient to restore biofilm formation to wild-type levels (Fig. 6b(v); wild-type biofilms were not affected by addition of IPTG; Fig. 6b(i–iii)). However, overexpression of GltAB (100 μM IPTG), resulted in a Δ*gudB*-like biofilm morphology (Fig. 6b(vi) and Extended Data Fig. 9b for enlarged images) consistent with silencing of GudB by GltAB. Expression of the inactive GltAB^{C1A} restored wild-type-like growth, but only in the interior of the biofilm resembling biofilms formed by Δ*gltB* strain (Fig. 6b(x–xii),c and Extended Data Fig. 9c for enlarged images), suggesting that silencing of GudB by GltAB is crucial for the interior of the biofilm. In contrast, if the GudB silencing occurs in the peripheral cells, the biofilm exhibits no wrinkles in the periphery (compared to wild-type, Fig. 6c). This result is also in agreement with GltAB's expression being the highest in the interior of the wild-type biofilm[34]. Indeed, when the above-described wild-type and inactive *gltAB* genes were expressed at the background of RocG, the effects differed completely from those seen at the GudB background (Fig. 6b(vii–ix, xiii–xv)). In the presence of RocG, expression of GltAB^{C1A} had no effect and the biofilms completely lacked wrinkles (Fig. 6c). This result is consistent with RocG having the same level of enzymatic activity as GudB, yet not being suppressed by GltAB binding. Overall, these results show besides enzymatically functional GudB and GltAB, regulation of GudB by GudB–GltAB counter-enzyme complex formation is critical to developing natural biofilm features.

Discussion

Our search for the regulatory mechanism of GudB, a core catabolic glutamate dehydrogenase that is constitutively expressed, yielded an unexpected answer. GudB, which is involved in glutamate catabolism, forms a transient complex with its counter enzyme GltAB, which catalyzes glutamate synthesis. The main purpose of this association seems to be silencing of GudB. The high-resolution structure of the partially assembled complex clearly showed that a regulatory loop in GltA occludes the active-site cleft of GudB and prevents cofactor binding. In addition, the structure revealed the mechanisms behind paralog specificity.

The GudB–GltAB complex presents a good case study for allosteric control of protomers in an oligomeric enzyme. GudB is active only as a hexamer and dimer/monomeric species are inactive[14,21]. The fact that physical association of GltA is needed for the inactivation of GudB protomer suggests that six GltA molecules are needed for the complete silencing of GudB (hexamer) and that in the partial complex, with substoichiometry GltA, the unbound GudB protomers could still be active. It should be noted that GudB by itself exhibits strong negative cooperativity ($H = 0.57$), and GltA-bound GudB exhibits weak yet reproducible positive cooperativity ($H = 1.3$) (Fig. 3c,d and Supplementary Table 2). This suggests that GltA binding does affect the intersubunit allosteric communication. Future studies focusing on substrate/product/cofactor bound structure of GudB and GudB–GltAB complex should shed light on the exact mechanism behind the strong negative cooperativity of GudB and modular control of GudB protomers by GltA binding.

A notable feature of the GudB–GltAB complex is the oscillatory progress curve. Oscillatory chemical reactions[35] and two-enzyme system has been described previously[36–40]. However, oscillations are not expected in a counter-enzyme pair. The rates of substrate binding, product release and catalytic turnover, are typically in the subsecond range and a steady state would therefore be established with a constant 'net' rate[24]. Mechanistically speaking, oscillations typically involve a negative feedback loop with a delay[24,41–43]. The delay is key for 'over-shooting' of one reaction before the next one takes over. While the GltA binding to GudB is the negative feedback here, the delay may be produced, for example, by any AKG-dependent slow event such as proline *cis–trans* isomerization in the regulatory

loop, global conformational change, domain motion or or by cycles of disassembly and slow reassembly of the complex. The last would result in GudB overproducing AKG due to a delay in GltAB's binding. That the oscillation frequency depends on the complex's concentration, and in a nonlinear way (Extended Data Fig. 3m–o), hints at such a mechanism. The GudB–GltAB oscillatory kinetics and the regulatory mode may also have some intriguing physiological implications in biofilms. Future work may therefore enable a deeper understanding of the GltAB–GudB complex, and also of the potential correlation between GudB's regulation and biofilm oscillations.

It was shown earlier that GudB/RocG can directly bind GltC (the transcriptional regulator of the GltAB operon) and repress GltAB expression[44]. This moonlighting function of GudB is undesirable in a glutamate-poor condition. It is therefore tempting to speculate that GudB–GltAB counter-enzyme complex formation is a fail-safe mechanism whereby, besides inhibiting the catalytic activity of GudB, it also sequesters GudB and prevent its interaction with GltC. The only other counter-enzyme complex reported previously is arginase–ornithine transcarbamylase (OTCase) complex where it was shown that the catabolic arginase inhibits the anabolic OTCase[45,46]. This is opposite of what we see in GudB–GltAB complex where the catabolic enzyme (GudB) is inhibited by the anabolic GltAB. Most biochemical transformations are in principle reversible. However, in vivo, many of these are effectively unidirectional due to thermodynamic and kinetic constraints. In addition, many enzymes evolved toward unidirectional catalysis, including oxidoreductases that use NAD^+ to drive the reaction in the oxidative direction (for example, GudB) or NADPH to direct reduction (for example, GltAB). Consequently, cells contain multiple counter enzymes that catalyze opposite transformations (note that the reactions themselves usually differ, as is the case with GltAB and GudB, but the primary substrate/product are the same as shown in Fig. 1a). It stands to reason that counter enzymes would be individually regulated, as their simultaneous operation could result in futile cycles (zero net outcome and waste of energy). However, regulation via counter-enzyme pairs offers unique properties that cannot be obtained by independent regulation of the individual enzymes, such as ultrasensitivity, robustness and temporal signaling pulses. The opposing enzymes can be separate proteins, or fused on the same polypeptide chain (bifunctional enzymes)[24]. The GudB–GltAB example unraveled here indicates that counter-enzyme pairs could be hotspots for regulatory features and warrants a systematic investigation of different counter-enzyme pairs in core metabolism.

Online content

Any methods, additional references, Nature Research reporting summaries, source data, extended data, supplementary information, acknowledgements, peer review information; details of author contributions and competing interests; and statements of data and code availability are available at https://doi.org/10.1038/s41589-021-00919-y.

Received: 28 May 2021; Accepted: 12 October 2021;
Published online: 20 December 2021

References

1. Chubukov, V. et al. Transcriptional regulation is insufficient to explain substrate-induced flux changes in *Bacillus subtilis*. *Mol. Syst. Biol.* **9**, 709 (2013).
2. Metallo, C. M. & Vander Heiden, M. G. Understanding metabolic regulation and its influence on cell physiology. *Molecular Cell* **49**, 388–398 (2013).
3. Curi, R. et al. Regulatory principles in metabolism: then and now. *Biochem. J* **473**, 1845–1857 (2016).
4. Srere, P. A. The metabolon. *Trends Biochem. Sci* **10**, 109–110 (1985).
5. Zhang, Y. & Fernie, A. R. Metabolons, enzyme–enzyme assemblies that mediate substrate channeling, and their roles in plant metabolism. *Plant Commun*. https://doi.org/10.1016/j.xplc.2020.100081 (2020).
6. Sweetlove, L. J. & Fernie, A. R. The role of dynamic enzyme assemblies and substrate channelling in metabolic regulation. *Nat. Commun*. **9**, 2136 (2018).
7. Lin, E. C. C., Lynch, A. S. & Magasanik, B. in *Regulation of Gene Expression in Escherichia coli* 281–290 (Springer, 1996).
8. Young, V. R. & Ajami, A. M. Glutamate: an amino acid of particular distinction. *J. Nutrition* **130**, 892S–900S (2000).
9. Yan, D., Ikeda, T. P., Shauger, A. E. & Kustu, S. Glutamate is required to maintain the steady-state potassium pool in *Salmonella typhimurium*. *Proc. Natl Acad. Sci. USA* **93**, 6527–6531 (1996).
10. Bennett, B. D. et al. Absolute metabolite concentrations and implied enzyme active site occupancy in *Escherichia coli*. *Nat. Chem. Biol.* **5**, 593–599 (2009).
11. Van Eunen, K. et al. Measuring enzyme activities under standardized in vivo-like conditions for systems biology. *FEBS J.* **277**, 749–760 (2010).
12. Tempest, D. W., Meers, J. L. & Brown, C. M. Influence of environment on the content and composition of microbial free amino acid pools. *J. Gen. Microbiol.* **64**, 171–185 (1970).
13. Huergo, L. F. & Dixon, R. The emergence of 2-oxoglutarate as a master regulator metabolite. *Microbiol. Mol. Biol. Rev.* **79**, 419–435 (2015).
14. Noda-Garcia, L., Romero Romero, M. L., Longo, L. M., Kolodkin-Gal, I. & Tawfik, D. S. Bacilli glutamate dehydrogenases diverged via coevolution of transcription and enzyme regulation. *EMBO Rep.* **18**, 1139–1149 (2017).
15. Commichau, F. M., Gunka, K., Landmann, J. J. & Stülke, J. Glutamate metabolism in bacillus subtilis: gene expression and enzyme activities evolved to avoid futile cycles and to allow rapid responses to perturbations of the system. *J. Bacteriol.* **190**, 3557–3564 (2008).
16. Belitsky, B. R. & Sonenshein, A. L. Role and regulation of *Bacillus subtilis* glutamate dehydrogenase genes. *J. Bacteriol.* **180**, 6298–6305 (1998).
17. Engel, P. C. A marriage full of surprises; forty-five years living with glutamate dehydrogenase. *Neurochem. Int.* **59**, 489–494 (2011).
18. Li, M., Li, C., Allen, A., Stanley, C. A. & Smith, T. J. The structure and allosteric regulation of mammalian glutamate dehydrogenase. *Arch. Biochem. Biophys.* **519**, 69–80 (2012).
19. Tomita, T., Kuzuyama, T. & Nishiyama, M. Structural basis for leucine-induced allosteric activation of glutamate dehydrogenase. *J. Biol. Chem.* **286**, 37406–37413 (2011).
20. Liu, J. et al. Metabolic co-dependence gives rise to collective oscillations within biofilms. *Nature* **523**, 550–554 (2015).
21. Gunka, K. et al. Functional dissection of a trigger enzyme: mutations of the *Bacillus subtilis* glutamate dehydrogenase RocG that affect differentially its catalytic activity and regulatory properties. *J. Mol. Biol.* **400**, 815–827 (2010).
22. Picossi, S., Belitsky, B. R. & Sonenshein, A. L. Molecular mechanism of the regulation of *Bacillus subtilis* gltAB expression by GltC. *J. Mol. Biol.* **365**, 1298–1313 (2007).
23. Smaldone, G. T. et al. A global investigation of the *Bacillus subtilis* iron-sparing response identifies major changes in metabolism. *J. Bacteriol.* **194**, 2594–2605 (2012).
24. Hart, Y. & Alon, U. The utility of paradoxical components in biological circuits. *Molecular Cell* **49**, 213–221 (2013).
25. Cottevieille, M. et al. The subnanometer resolution structure of the glutamate synthase 1.2-MDa hexamer by cryoelectron microscopy and its oligomerization behavior in solution: functional implications. *J. Biol. Chem.* **283**, 8237–8249 (2008).
26. Swuec, P., Chaves-Sanjuan, A., Camilloni, C., Vanoni, M. A. & Bolognesi, M. Cryo-EM structures of *Azospirillum brasilense* glutamate synthase in its oligomeric assemblies. *J. Mol. Biol.* **431**, 4523–4526 (2019).
27. Vanoni, M. A. & Curti, B. Glutamate synthase: a complex iron-sulfur flavoprotein. *Cell Mol. Life Sci.* **55**, 617–638 (1999).
28. Kameya, M. et al. A novel ferredoxin-dependent glutamate synthase from the hydrogen-oxidizing chemoautotrophic bacterium *Hydrogenobacter thermophilus* TK-6. *J. Bacteriol.* **189**, 2805–2812 (2007).
29. Stillman, T. J., Baker, P. J., Britton, K. L. & Rice, D. W. Conformational flexibility in glutamate dehydrogenase. *J. Mol. Biol.* **234**, 1131–1139 (1993).
30. Prakash, P., Punekar, N. S. & Bhaumik, P. Structural basis for the catalytic mechanism and -ketoglutarate cooperativity of glutamate dehydrogenase. *J. Biol. Chem.* **293**, 6241–6258 (2018).
31. Hassanov, T., Karunker, I., Steinberg, N., Erez, A. & Kolodkin-Gal, I. Novel antibiofilm chemotherapies target nitrogen from glutamate and glutamine. *Sci. Rep.* **8**, 1–12 (2018).
32. Pisithkul, T. et al. Metabolic remodeling during biofilm development of *Bacillus subtilis*. *mBio* **10**, e00623-19 (2019).
33. Zhang, N. et al. Whole transcriptomic analysis of the plant-beneficial rhizobacterium *Bacillus amyloliquefaciens* SQR9 during enhanced biofilm formation regulated by maize root exudates. *BMC Genomics* **16**, 685 (2015).
34. Liu, J. et al. Coupling between distant biofilms and emergence of nutrient time-sharing. *Science* **356**, 638–642 (2017).
35. Noyes, R. M. & Field, R. J. Oscillatory chemical reactions. *Annu. Rev. Phys. Chem.* **25**, 95–119 (1974).
36. Goldbeter, A. Mechanism for oscillatory synthesis of cyclic AMP in *Dictyostelium discoideum*. *Nature* **253**, 540–542 (1975).

37. Rossomando, E. F. & Sussman, M. A 5'-adenosine monophosphate-dependent adenylate cyclase and an adenosine 3':5'-cyclic monophosphate-dependent adenosine triphosphate pyrophosphohydrolase in *Dictyostelium discoideum*. *Proc. Natl Acad. Sci. USA* **70**, 1254–1257 (1973).
38. Pálsson, E. A cAMP signaling model explains the benefit of maintaining two forms of phosphodiesterase in *Dictyostelium*. *Biophys. J.* **97**, 2388–2398 (2009).
39. Masaki, N., Fujimoto, K., Honda-Kitahara, M., Hada, E. & Sawai, S. Robustness of self-organizing chemoattractant field arising from precise pulse induction of its breakdown enzyme: a single-cell level analysis of pde expression in dictyostelium. *Biophys. J.* **104**, 1191–1202 (2013).
40. Nakajima, M. et al. Reconstitution of circadian oscillation of cyanobacterial KaiC phosphorylation in vitro. *Science* **308**, 414–415 (2005).
41. Wagner, A. Circuit topology and the evolution of robustness in two-gene circadian oscillators. *Proc. Natl Acad. Sci. USA* **102**, 11775–11780 (2005).
42. Radde, N. The impact of time delays on the robustness of biological oscillators and the effect of bifurcations on the inverse problem. *Eurasip J. Bioinforma. Syst. Biol.* **2009**, 327503 (2009).
43. Blanchini, F., Cuba Samaniego, C., Franco, E. & Giordano, G. Homogeneous time constants promote oscillations in negative feedback loops. *ACS Synth. Biol.* **7**, 1481–1487 (2018).
44. Commichau, F. M., Herzberg, C., Tripal, P., Valerius, O. & Stülke, J. A regulatory protein–protein interaction governs glutamate biosynthesis in *Bacillus subtilis*: the glutamate dehydrogenase RocG moonlights in controlling the transcription factor GltC. *Mol. Microbiol.* **65**, 642–654 (2007).
45. Messenguy, F. & Wiame, J. M. The control of ornithinetranscarbamylase activity by arginase in *Saccharomyces cerevisiae*. *FEBS Lett.* **3**, 47–49 (1969).
46. Messenguy, F., Penninckx, M. & Wiame, J. -M. Interaction between arginase and ornithine carbamoyltransferase in *Saccharomyces cerevisiae*: the regulatory site for ornithine. *Eur. J. Biochem.* **22**, 277–286 (1971).

Methods

DNA manipulation. All constructs used for genome modification were generated using Gibson assembly. The starting fragments were generated using Q5 High-Fidelity DNA Polymerase (New England Biolabs) and NEBuilder HiFi DNA Assembly Master Mix (New England Biolabs) was used for assembly. The linear DNA fragments for *B. subtilis* transformation were generated by digestion of the plasmids (using a single restriction enzyme) or by PCR using the Gibson assembly reaction as template. The fragments had recombination homology arms ranging anywhere from 1.5 to 4 kb. All the strains generated and used in the study are listed in Supplementary Table 6 and all the oligonucleotides used for the study are listed in Supplementary Table 7. Genetic modification of *B. subtilis* strains were performed based on natural competence: the parental strains were streaked on a Luria-Bertani (LB) agar plate and grown overnight at 37 °C. A singly colony was then used to inoculate 1 ml of modified competance medium (MC)[47] containing 0.5% glucose, 1.4% K_2HPO_4, 0.6% KH_2PO_4, 30 nM sodium citrate tribasic dehydrate, 0.2% casein hydrolysate, 84 mM ammonium iron(III) citrate and 3 µM $MgSO_4$. Addition of tryptophan (0.005%) and histidine (0.005%), improved the transformation efficiency. The culture was incubated at 37 °C in a roller drum shaker for 3.5 h. Linear DNA/genomic DNA (100 ng–1 µg) was added to 300 µl of this culture and growth was continued for another 3 h. The positive transformants were selected either on an antibiotic, or in nutrient selection media (for wild-type GltAB constructs). All transformants were verified by diagnostic PCRs followed by DNA sequencing.

Media and growth conditions. *B. subtilis* strains were grown in LB or in Murashige and Skoog medium (5 mM potassium phosphate, 100 mM MOPS pH 7.1, 2 mM $MgCl_2$, 700 µM $CaCl_2$, 50 µM $MnCl_2$, 50 µM $FeCl_3$, 1 µM $ZnCl_2$ and 2 µM thiamine; adapted from ref. [48]). The medium was supplemented with appropriate carbon/nitrogen source (glutamate, histidine, arginine, proline) or with a carbon source (glucose, glycerol) plus ammonium sulfate, all at a final concentration of 5 g l^{-1}. Media were supplemented with antibiotics when required: kanamycin (10 µg ml^{-1}), tetracycline (5 µg ml^{-1}), spectinomycin (100 µg ml^{-1}) or a mix of lincomycin (25 µg ml^{-1}) plus erythromycin (2 µg ml^{-1}). Growth profiling of *B. subtilis* strains in liquid Murashige and Skoog medium was performed in a 96-well plates and absorbance at an optical density of 600 nm (OD_{600}) was measured using a multiwell plate reader (Eon, Biotek Gen5). Typically, 3 µl of culture with an OD_{600} of 0.8–1.2 was used as a starter to inoculate a well containing 200 µl of fresh medium. Replicates were performed in parallel in the same plate.

For biofilm growth, the Murashige and Skoog media (supplemented with appropriate C/N source) was solidified using 1.5% agar (w/v). The plates were then dried for 6–8 h in a laminar hood. For biofilm growth, cells stocks were streaked on to an LB agar plate and incubated overnight at 37 °C. From the confluent part of the plate, cells were swiped using a sterile loop to inoculate 5 ml of LB medium, then grown at 37 °C and shaken for 2–3 h (OD_{600} of 0.8–1.2). Following this the cells were washed twice with 1× PBS. The cultures were normalized based on OD_{600} and a 3 µl aliquot of a 0.6–1.0 OD_{600} culture was placed at the center of the plate for biofilm growth, and the plates were incubated at 30 °C. Photographs of the biofilms were acquired using Stereo Discovery V20 microscope with an Objective Plan Apo S ×0.5 FWD 134 mm or Apo S ×1.0 FWD 60 mm (Zeiss) attached to an Axiocam camera. Data were captured and analyzed using ZENpro AxioVision suite software (Zeiss).

Immunoprecipitation and mass spectrometry. Anti-GudB antibodies were generated in rabbits using recombinant GudB purified from *Escherichia coli* as antigen. The IgG fraction from these polyclonal sera was purified using a Protein A column. The purified antibodies were covalently linked to CNBr beads[49] and this resin was used for the pulldown of GudB from *B. subtilis* cell lysates. Briefly, wild-type *B. subtilis* (NCIB 3610) was grown in 500 ml of Murashige and Skoog medium supplemented with either glucose ammonia or histidine. Cells were gathered by centrifugation (6,100 relative centrifugal force (rcf)) and resuspended in 30 ml of lysis buffer (100 mM Tris. HCl, 150 mM NaCl, EDTA-free protease cocktail inhibitor (1:200, Abcam), 2 mM dithiothreitol (DTT)). The cells were lysed by passing cell suspensions 3–4 times through a french press at a pressure of 15 psi. The debris were removed by centrifugation (11,648 rcf) and the resulting supernatant was mixed with the anti-GudB antibodies resin and incubated for 1 h. After rinsing the beads, the bound proteins were eluted using a low-pH glycine buffer (100 mM, pH 2.8). Eluates were neutralized by collecting them directly into 2 M Tris buffer pH 8.5, pooled and lyophilized. The eluted proteins were resolved on SDS–PAGE and stained with silver nitrate using established protocols[50].

For MS-based identification of proteins, the dried eluates were resuspended in 5% SDS in 50 mM Tris pH 7.4 and subjected to tryptic digestion using an S-trap[51]. The resulting peptides were analyzed using nanoflow liquid chromatography (Acquity M-class) coupled to high-resolution, high mass accuracy mass spectrometry (Q-Exactive HF). Each sample was analyzed on the instrument separately, in a random order, discovery mode. Raw data were processed with MaxQuant v.1.6.0.16, and searched with the Andromeda search engine against the *B. subtilis* proteome database appended with common laboratory protein contaminants, with the following modifications: carbamidomethylation of cysteine as a fixed modification and oxidation of methionine as a variable one. The label-free quantification intensities were calculated and used for further calculations using Perseus v.1.6.0.7. Decoy hits were filtered out, as well as proteins that were identified on the basis of a modified peptide only.

Protein expression and purification. Recombinant GudB and RocG were purified as described[14]. Briefly, the plasmids pET28_Strep_GudB and pET28_Strep_RocG encoding *B. subtilis* GudB and RocG respectively, were used for expression in the *E. coli* strain BL21 star/DE3 (pGRO7). Typically, the cells were grown in 1 l of terrific broth supplemented with kanamycin (50 µg ml^{-1}) and chloramphenicol (34 µg ml^{-1}) to an OD_{600} of 0.6–0.8 and protein expression was induced by the addition of 100 µM IPTG. Postinduction, the cultures were grown overnight at 20 °C with shaking (200 r.p.m.). Cells were gathered by centrifugation (6,100 rcf), resuspended in lysis buffer (100 mM Tris. HCl, 150 mM sodium chloride, protease cocktail inhibitor) and lysed using a french press at 15 psi. The clarified cell lysate was applied on to a Strep-Tactin column, unbound proteins were removed by washing with 5 CV of lysis buffer, and the target protein was eluted using 10 mM desthiobiotin in lysis buffer. The eluted protein was then dialyzed overnight in storage buffer (50 mM HEPES pH 7.9); aliquots were flash frozen in liquid nitrogen and stored at −80 °C in a freezer for later use.

The GudB–GltAB complex was purified directly from *B. subtilis* strain in which GltB is expressed as a Twinstrep-tagged protein (GltB-TS). For the purification of GltAB alone without GudB, the Δ*gudB* version of the strain expressing GltB-TS was used. A higher yield of the complex was obtained on using strains containing *gltAB* genes under an IPTG-inducible hyperspank promoter. GltAB contains Fe-S clusters that are essential for its activity; to prevent cluster oxidation, all buffers used for the purification were degassed first by applying vacuum and then purging the solution with nitrogen for roughly 40 min. additionally, the buffer was supplemented with 5 mM DTT to maintain reducing conditions. For purification, the relevant *B. subtilis* strain was grown in 1–2 l of Murashige and Skoog medium containing glucose ammonia to an OD_{600} of 1.5–2. The cells were collected by centrifugation, resuspended in lysis buffer (100 mM Tris. HCl, 150 mM sodium chloride, protease cocktail inhibitor, 2 mM DTT) and lysed using a french press. The clarified cell lysate was either directly applied on to a Strep-Tactin column or in the case of a GudB-enriched sample, the lysate was incubated with lysate from the *E. coli* overexpressing 6× His-tagged GudB. The column was washed with 5 CV of lysis buffer and the bound proteins were eluted using lysis buffer containing 10 mM of desthiobiotin. Elution aliquots were immediately flash frozen and stored at −80 °C. Quantification of the eluates were performed using Bradford assay (BioRad). The concentration of individual proteins in the complex was determined by densitometric analysis on ImageJ2 (ref. [52]).

Paralog-specific binding of GltAB was tested by pulldown of GltB-TS from a strain expressing either RocG or GudB. Cell lysates from the respective strains were applied onto a Strep-Tactin column, unbound proteins washed and the bound proteins eluted using 10 mM desthiobiotin in lysis buffer. The proteins in the eluate were separated on SDS–PAGE and Coomassie stained. For the reciprocal pulldown, purified recombinant 6× His RocG or GudB were added to *B. subtilis* cell lysates containing GltAB-TS. Bound proteins were pulled down as above. Interactions were also tested in vitro, by adding either recombinant 6× His-tagged GudB/RocG to *B. subtilis* cell lysates containing GltAB-TS. The lysate was applied on to a Ni-NTA column and the column was washed with 10 CV of wash buffer. Proteins bound to the column were eluted using 500 mM imidazole in lysis buffer. The eluates were resolved on SDS–PAGE and the gel was visualized using Coomassie staining.

Crosslinking and western blotting. Disuccinimidyl glutarate was synthesized using established protocols. Briefly, glutaric acid (2.0 g, 1.0 eq.) and *N*-hydroxy succinimide (3.8 g, 2.2 eq) were added to an oven dried round bottom flask containing 30 ml of dimethylformamide and kept on ice. Then, EDC.HCl (6.4 g, 2.2 eq) was added to the flask on ice and the reaction was subsequently stirred at room temperature overnight. The reaction mixture was then poured onto an ice-cold solution of 1 N HCl (roughly 10 volumes) and stirred for a few minutes. The resultant solution was filtered and the precipitate was rinsed twice with ice-cold isopropanol. The obtained solids were dried under a vacuum and further lyophilized to remove traces of water. The lyophilized powder was stored at −20 °C. For crosslinking, wild-type *B. subtilis* strain NCIB 3610 was grown in 10 ml of Murashige and Skoog medium supplemented with appropriate C/N source to an OD_{600} of 1–1.5. Cells were gathered by centrifugation and washed with 1× PBS. The cells were resuspended in 500 µl of 1× PBS. DSG was prepared freshly by dissolving it in anhydrous dimethylsulfoxide to 250 mM, and added to the cell suspension to a final concentration of 0.5–2 mM. The cells were incubated in a tumbler, at room temperature, for 30 min unless otherwise specified. The crosslinking reaction was stopped by the addition of 2 M Tris pH 8.5 (to a final concentration of 150 mM) and incubated for another 15 min. The cells were collected by centrifugation and the cell pellets stored at −20 °C.

For western blotting, the pellets of DSG-treated/untreated cells were resuspended in 1× SDS–PAGE loading dye and heated at 95 °C for 15 min. The cell debris was removed by centrifugation and the supernatant was analyzed on 8 or 12% SDS–PAGE gel. The loading was normalized based on OD_{600} of the culture before crosslinking. The resolved proteins were transferred onto a polyvinyl

difluoride membrane and blocked with 5% skim milk solution in 1× PBS at room temperature for 1 h. Anti-GudB antibody (Protein A purified) was added (1:50,000) to the blocking solution and the membrane was incubated for 1 h. Following this, the membrane was subjected to three wash cycles, 5 min each, in washing buffer containing 0.01% Tween (in 1× PBS). Following the washes, HRP-conjugated antirabbit IgG (Jackson ImmunoResearch, 111-035-144), was added (1:50,000) and incubated with shaking for 1 h. The blot was washed again and the protein bands were visualized using the ECL system and images acquired in Amersham imager 680, General Electric Company.

Enzyme kinetics. Glutamate dehydrogenase and glutamate synthase activities were monitored by a change in absorbance at 340 nm. While the dehydrogenase reaction involves NAD^+ reduction and hence increase in absorbance as the reaction proceeds, the synthetase reaction involves NADPH oxidation and decrease in absorbance. All kinetic assays were performed in multiwell plates suitable for measuring in ultraviolet (UV) range (Microplate UV/VIS 96F, Eppendorf). Reactions were performed in 50 mM HEPES buffer pH 7.9, at a total volume of 200 µl, and were initiated by enzyme addition (5 µg of recombinant GudB and 2.5 µg of GudB–GltAB complex). Steady-state kinetic parameters for the enzymes were derived from initial velocity measurements where one substrate was titrated keeping all other substrates saturating. For GudB, the saturating concentration for glutamate was 200 mM, and for NAD^+, 4 mM. For GltAB, the saturating concentrations of glutamine was 100 mM, AKG, 2 mM and NADPH 200 µM. In addition to these substrates, all reactions involving GltAB included 5 mM $MgSO_4$ and 5 mM DTT. The data were fitted to Michaelis–Menten or to an allosteric sigmoidal model in GraphPad Prism (v.9.1.0).

Native MS. All native MS measurements were preformed using Q-Exactive UHMR instrument (Thermo Fisher Scientific). Before the analysis, samples were buffer exchanged into 150 mM of ammonium acetate pH 8 using Bio-Spin P6 columns (BioRad) and the final protein concentrations were adjusted to 1–5 µM. The following parameters were used for the MS1 experiment: capillary voltage 1,100, desolation voltage −100 V, source fragmentation 0 V, HCD energy 50 V, trapping pressure 7, corresponding to high vaccuum (HV) pressure of 2.04×10^{-4} mbar. All spectra were recorded at resolution of 6250 at 800 *m/z* and analyzed using Xcalibur and Masslynx v.4.2 (Waters) data analysis software. Spectra are shown without any smoothing, and the instrument were externally mass calibrated using a 2 mg ml^{-1} cesium iodide solution.

Cryo-EM sample preparation. Both $GudB_6$-$GltA_2B_2$ and $GudB_6$-$GltA_6B_6$ protein samples were prepared at a protein concentration of 0.5 mg ml^{-1} and applied to glow discharged R 2/2, 300 mesh, grids with an additional thin layer (roughly 2 nm) of continuous carbon (Quantifoil). The $GudB_6$–$GltA_2B_2$ complex solution was applied to the grid in a single 2.5-µl drop, followed by 30 s of incubation before blotting. The $GudB_6$–$GltA_6B_6$ sample was applied in two consecutive drops of 6 and 3 µl to increase complex concentration on the grid. The first drop was blotted manually, followed by application of the second drop and automated blotting in the plunger. Both samples were plunge frozen in liquid ethane cooled by liquid nitrogen using a Vitrobot plunger (Thermo Fisher Scientific). The plunger was set to 3 s blotting time and 100% humidity.

Cryo-EM data collection. Data collection and statistics are summarized in Supplementary Table 5 and Extended Data Figs. 4 and 6. Cryo-EM data were collected on a Titan Krios G3i transmission electron microscope (Thermo Fisher Scientific) operated at 300 kV. Videos were recorded on a K3 direct detector (Gatan) installed behind a BioQuantum energy filter (Gatan), using a slit of 15 eV. Videos were recorded in counting mode at a nominal magnification of ×105,000, corresponding to a physical pixel size of 0.82 Å. The $GudB_6$–$GltA_6B_6$ data set was collected at a dose rate of 21.4 e^- pixel^{-1} s^{-1} and total exposure time of 1.5 s, resulting in an accumulated dose of 47.7 e^- Å^2. The $GudB_6$–$GltA_2B_2$ data set was collected at a dose rate of 20.5 e^- pixel^{-1} s^{-1} and total exposure time of 2 s, resulting in an accumulated dose of 61 e^- Å^2. Each video was split into 60 frames, and the nominal defocus range was −0.8 to −2 µm. Each video was split into 45 frames, and the nominal defocus range was −0.7 to −1.8 µm. The microscope was optically aligned for fringe-free illumination[53], enabling reduction of the beam diameter to 0.7 µm on the sample. Imaging was done using an automated low dose procedure implemented in SerialEM[54], in which image shift was used to collect multiple images within a single hole. The beam tilt was adjusted to achieve coma-free alignment when applying image shift.

Cryo-EM image processing and model building. The $GudB_6$–$GltAB_2$ Coulomb potential density map was reconstructed in cisTEM (v.1.0.0-beta) using dose-weighted micrographs. These were prepared by binning the image stacks by a factor of 2, correcting for beam-induced motion and dose-weighting with MotionCor2 (v.1.3.0). Contrast transfer function (CTF) estimation was performed using CTFFIND4 as part of the cisTEM suite. Micrographs with crystalline ice and poor CTF fits were discarded. Particles were picked in cisTEM using a featureless blob as a template, then were extracted and classified in two dimensions. All nonice classes were carried forward to a two-class 3D auto-refinement, using an initial reference produced by a cryoSPARC ab initio and the default starting resolution of 20 Å. The auto-refinement yielded one 'noise' class containing poorly aligned particles and one class containing the $GudB_6$–$GltAB_2$ complex. Particles from this class were carried forward in a single-class 3D auto-refinement, followed by manual refinement with C2 symmetry and per-particle CTF correction. To prevent overrefinement, a final high-resolution limit of 3.14 Å was used. The final cisTEM map was auto-sharpened in PHENIX (v.1.19).

Image processing of the $GudB_6$-$GltA_6B_6$ data set was performed using CryoSPARC (v.3.1.0)[55]. The processing scheme is outlined in Extended Data Fig. 4. Videos were subjected to patch motion correction, followed by patch CTF estimation. Micrographs with crystalline ice or poor CTF fits were discarded. Particles were initially picked manually from a subset of micrographs. Extracted particles were iteratively classified in two dimensions and their class averages used as templates for automated particle picking from all selected micrographs. The latter procedure was repeated twice. Particles from well-resolved two-dimensional (2D) classes were used for ab initio 3D reconstruction and classification, yielding four 'noise' 3D classes and one class containing the $GudB_6$–$GltA_6B_6$ complex. Particles from this class were carried forward in a 3D nonuniform refinement with imposed D3 symmetry, followed by an additional round of 3D classification to further exclude 'noise' particles. The data set was then subjected to local motion correction, per-particle defocus estimation and nonuniform refinement with D3 symmetry. To account for movements of asymmetric units within the complex that break the D3 symmetry, we used the 'symmetry expansion' job in CryoSPARC, in which asymmetric units are treated as single particles and rotated in 2D to one of the symmetry-related positions. The newly generated data set contains the asymmetric units of all the complexes and is therefore six times larger. Symmetry expansion was followed by 3D local refinement of the newly generated data set with a binary mask imposed on a single $GudB_1$–$GltA_1B_1$ unit and with C1 symmetry. The final map was sharpened in CryoSPARC with a B-factor of −127 before atomic model building.

The initial model for GudB was extracted from PDB 3K8Z, but modified to reintroduce the Q71 residue that appears to be missing in GudB's published structure. Initial models for GltA and GltB were prepared by homology modeling (SWISS-MODEL) using PDB 1OFD, chain A, as the template for GltA and PDB 6S6T, chain G, as the template for GltB. These models were aligned with the Coulomb potential density map for $GudB_6$–$GltA_2B_2$ using rigid body docking (UCSF Chimera v.1.14) then refined by performing iterative rounds of manipulation in ISOLDE (ChimeraX v.1.1.1, ISOLDE v.1.1.0), Coot (v.0.9.3) and phenix.real_space_refine (v.1.19). The final round of refinement was with phenix.real_space_refine (v.1.19). From the $GudB_6$–$GltA_2B_2$ model, one set of monomers was extracted and refined into the C1 map for the $GudB_6$–$GltA_6B_6$ data set described in the previous paragraph. Refinement similarly involved a round of ISOLDE (ChimeraX v.1.1.1, ISOLDE v.1.1.0), Coot (0.9.3) and phenix.real_space_refine (1.19). To produce the biological assembly, the $GudB_1$–$GltA_1B_1$ model was expanded into the full D3 map by applying noncrystallographic symmetry and rigid body docking. The models were inspected in Coot (v.0.9.4.1), ChimeraX (v.1.1.1) and pyMol (v.2.4.1). 3D visualization was performed using UCSF Chimera (v.1.14).

Mass photometry. The mass photometry data were acquired using a One^{MP} mass photometer (Refeyn Ltd). The procedure used was based on previous published protocols[56]. Briefly, washed and dried gaskets (with chambers for holding the protein solution) was assembled on a clean coverslip. Then 16 µl of 50 mM HEPES buffer was loaded in one of the chambers and this was used to find focus. To this, 4 µl of protein solution (calibrant/test protein) was added and the video recorded for a period of 120 s. A 50 nM solution of urease was used for mass calibration. GltAB alone was used at a final concentration of 50 nM or mixed with AKG and NADPH at final concetrations of 5 and 200 µM, respectively. The videos were processed and analyzed using Discover^{MP}.

Metabolite extraction and analysis. Lyophilized protein pellets were mixed with 100 µl of methanol:double distilled water (DDW), 1:1 (v/v). Samples were vortexed for 10 min and sonicated for 15 min. Then the samples were centrifuged twice (at maximum speed) to remove possible precipitants and were injected into a liquid chromatography–mass spectrometry system. We carried out metabolite analysis using Acquity I class ultra-performance liquid chromagraphy system combined with a mass spectrometer (Thermo Exactive Plus Orbitrap), which was operated in a negative ionization mode. Liquid chromatography separation was performed using the SeQuant Zic pHilic (150 × 2.1 mm) with the SeQuant guard column (20 × 2.1 mm) (Merck). The mobile phase B was acetonitrile and mobile phase A was 20 mM ammonium carbonate with 0.1% ammonia hydroxide in water:acetonitrile (80:20, v/v). The flow rate was maintained at 200 µl min^{-1}, and the gradient was: 0–2 min 75% of B, 17 min 12.5% of B, 17.1 min 25% of B, 19 min 25% of B, 19.1 min 75% of B, 23 min 75% of B. The data processing was done using Thermo Scientific Xcalibur v.4.1.31.9 software. Compounds were identified by accurate mass, retention time, isotope pattern, fragments and verified using an in-house mass spectra library.

Reporting Summary. Further information on research design is available in the Nature Research Reporting Summary linked to this article.

Data availability

The proteomics data are provided as Excel sheets (Supplementary Datasets 1 and 2). The structural data are deposited in the PDB (PDB codes 7MFM and 7MFT). Source data are provided with this paper.

References

47. Wilson, G. A. & Bott, K. F. Nutritional factors influencing the development of competence in the *Bacillus subtilis* transformation system. *J. Bacteriol.* **95**, 1439–1449 (1968).
48. Branda, S. S., González-Pastor, J. E., Ben-Yehuda, S., Losick, R. & Kolter, R. Fruiting body formation by *Bacillus subtilis*. *Proc. Natl Acad. Sci. USA* **98**, 11621–11626 (2001).
49. Kavran, J. M. & Leahy, D. J. in *Laboratory Methods in Enzymology* Vol. 541 (ed. Lorsch, J.) 27–34 (Academic Press Inc., 2014).
50. Kavran, J. M. & Leahy, D. J. in *Laboratory Methods in Enzymology* Vol. 541 (ed. Lorsch, J.) 169–176 (Academic Press Inc., 2014).
51. Elinger, D., Gabashvili, A. & Levin, Y. Suspension trapping (S-Trap) is compatible with typical protein extraction buffers and detergents for bottom-up proteomics. *J. Proteome Res.* **18**, 1441–1445 (2019).
52. Rueden, C. T. et al. ImageJ2: ImageJ for the next generation of scientific image data. *BMC Bioinf.* **18**, 529 (2017).
53. Konings, S. et al. Advances in single particle analysis data acquisition. *Microsc. Microanal.* https://doi.org/10.1017/s1431927619005798 (2019).
54. Mastronarde, D. N. Automated electron microscope tomography using robust prediction of specimen movements. *J. Struct. Biol.* https://doi.org/10.1016/j.jsb.2005.07.007 (2005).
55. Punjani, A., Rubinstein, J. L., Fleet, D. J. & Brubaker, M. A. CryoSPARC: algorithms for rapid unsupervised cryo-EM structure determination. *Nat. Methods* https://doi.org/10.1038/nmeth.4169 (2017).
56. Sonn-Segev, A. et al. Quantifying the heterogeneity of macromolecular machines by mass photometry. *Nat. Commun.* **11**, 1772 (2020).

Acknowledgements

We thank K.P. Cherukuri for help in synthesis of DSG, A. Leytens for assistance in cloning and Y. Kushmaro for screening different crosslinkers. We are grateful to M. Kupervaser and Y. Levin from The De Botton Protein Profiling institute of the Nancy and Stephen Grand Israel National Center for Personalized Medicine, Weizmann Institute of Science, for the proteomics analysis. We thank A. Sonn Segev and M. Goldsmith for their assistance with the mass photometry experiments. We thank S. Malitsky and M. Itkin for the metabolomics analysis. We thank U. Sauer, U. Alon, N. Tokuriki and S. Laxman for their critical feedback on the paper. We thank F. Jonas for valuable comments on the paper and B. Ross for proofreading. Funding by the Israel Science Foundation grant no. 2575/20 is gratefully acknowledged. M.S. is the incumbent of the Aharon and Ephraim Katzir Memorial Professorial Chair. The research by S.V. is supported by the Clore Israel Foundation. J.S.F. is supported by National Institutes of Health (NIH) grant no. GM123159 and D.J.L. is supported by NIH grant no. F32 AI148120. D.S.T. is the incumbent of the Nella and Leon Benoziyo Professorial Chair.

Author contributions

D.S.T. conceptualized the study and supervised all research. V.J. performed all experimental work unless otherwise stated. S.V. performed the native MS and M.S. supervised this analysis. N.E. acquired the cryo-EM data. D.J.L., V.J. and N.E. performed the cryo-EM data processing and model building. This was supervised by J.S.F. V.J., J.S.F. and D.S.T wrote the paper and all authors reviewed the data and the paper.

Competing interests

The authors declare no competing interests.

Additional information

Extended data are available for this paper at https://doi.org/10.1038/s41589-021-00919-y.

Supplementary information The online version contains supplementary material available at https://doi.org/10.1038/s41589-021-00919-y.

Correspondence and requests for materials should be addressed to Vijay Jayaraman or James S. Fraser.

Peer review information *Nature Chemical Biology* thanks Marcus Hartmann, Jörg Stülke and Ramaswamy Subramanian for their contribution to the peer review of this work.

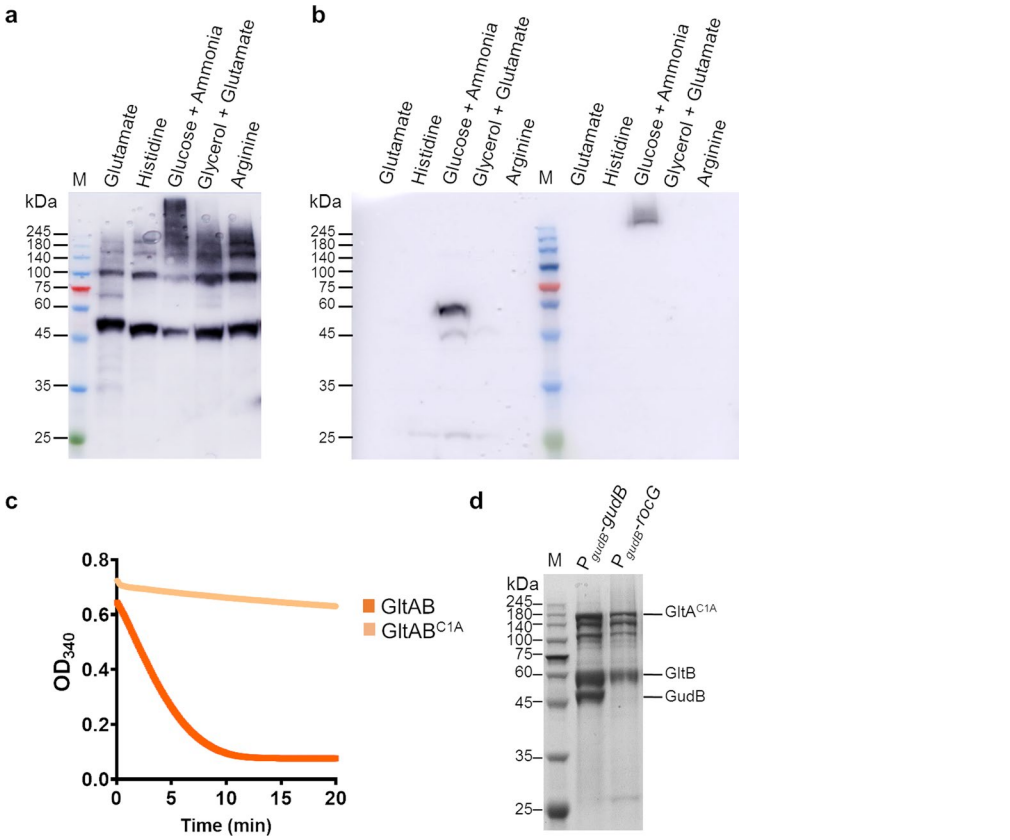

Extended Data Fig. 1 | GudB interacts with GltAB. (a) Western blot analysis using an anti-GudB antibody on lysates prepared from DSG treated *B. subtilis* cells grown on different C/N source. The high molecular weight species of GudB are seen only in cells grown in glucose⁻ammonia. **(b)** Western blot analysis using a Strep-Tactin-HRP antibody on the same samples used in A. Here the antibody was used on lysates prepared from both DSG-treated (lanes right to the molecular weight marker) and untreated cells (lanes left to the marker). As, can been seen, GltB is expressed only in cells grown on glucose⁻ammonia, and under this condition, it is also part of a high-MW complex (in the DSG treated sample) (Fig. 1b**)**. **(c)** Enzyme kinetics of wild-type GltAB (orange) and its mutant GltAB^{C1A} (light orange), show that the mutant is completely inactive. A minor decrease in absorbance with mutant GltA is due to non-enzymatic oxidation of NADPH. The reaction mixture consisted of 2 mM AKG, 5 mM glutamine, 200 µM NADPH, 5 mM DTT, 5 mM $MgSO_4$. The reaction was initiated with 2.5 µg of the wild-type or mutant enzyme. **(d)** SDS-PAGE of the eluate from Strep-Tactin column to which lysate from *B. subtilis* strain expressing GltAB^{C1A} in the background of constitutively expressed GudB or RocG is applied. Co-elution of GudB along with the inactive GltA (GltAB^{C1A}) upon pulldown of Strep-GltB (P_{gudB}-*gudB* lane), while GltAB^{C1A} elutes on its own when expressed with RocG (P_{gudB}-*rocG* lane). Images in a-d are obtained from a single experiment and are a representative of at least 2 independent experiments.

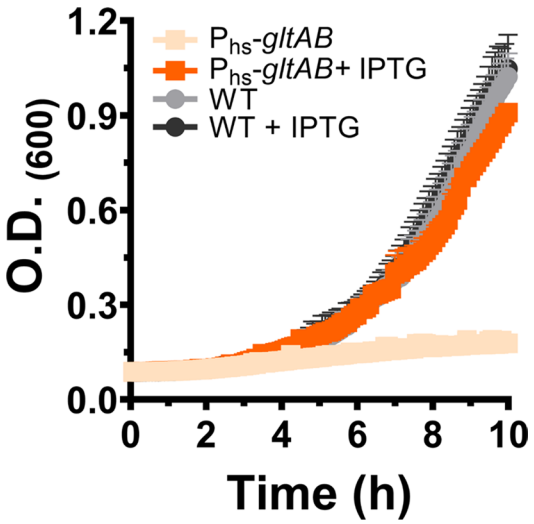

Extended Data Fig. 2 | Phenotyping of Phs-gltAB strain. The strain expresses GltAB from the IPTG- inducible hyperspank (P_{hs}) promoter. Without IPTG, the strain cannot grow in minimal medium containing glucose–ammonia as the C/N source (light orange); however, addition of 500 μM IPTG restores growth to almost wild-type levels (orange). Addition of IPTG does not have any effect on the growth of the parental wild-type strain. n = 3 are three independent measurements. Data is presented as mean of all measurements and error bars represent SD.

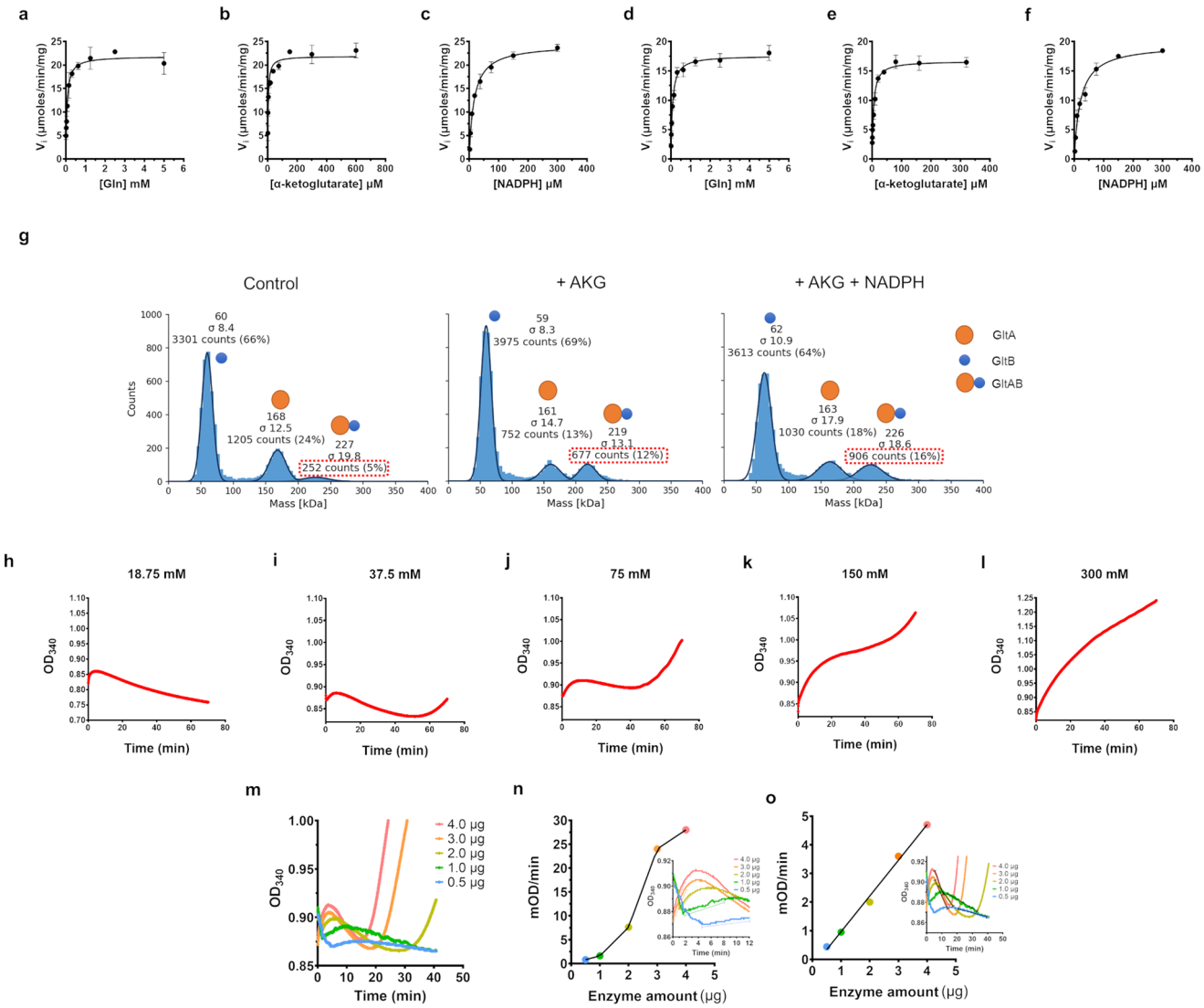

Extended Data Fig. 3 | Steady-state kinetics of GltAB, and GudB–GltAB complex. (a-f) Substrate titration plots for the glutamate synthase activity of GltAB by itself (A-C) and in the GudB bound form (D-F). One of the substrates was titrated while keeping the rest saturating: glutamine (5 mM), AKG (α-ketoglutarate, 2 mM), NADPH (200 μM). n = 2 are two independent experiments. Data is presented as mean and error bars indicate SD. **(g)** AKG and NADPH promote the assembly of GltA and GltB. Only 5 % of the counts corresponded to GltAB when no ligands were added (left panel). Addition of AKG increase the GltAB count to 12 % (Middle panel) and the presence of NADPH in addition to AKG increased the GltAB counts to 16 % (right panel). **(h-l)** Non-hyperbolic progress curves displayed by GudB-GltAB complex in the presence of all the substrates except AKG. While at high glutamate concentrations GudB's activity dominates (K), at low glutamate concentration the synthase activity takes over (G). At intermediate concentration of glutamate (H- J) the progress curve oscillates between GudB- and GltAB-predominant phases. **(m)** Progress curves obtained using different amount of the GudB-GltAB complex at 37.5 mM glutamate (where oscillations are most pronounced; **panel i**). The reaction mixture contained all substrates for GudB and GltAB except AKG. **(n)** Plotted are the slopes derived from phase 2 of the progress curves (GudB's activity as shown in the inset) as a function of the complex concentration. The non-linear relationship suggest that association-dissociation of the complex plays a role in turning off-on GudB's activity. Note also the elapsed time for phase 2 (the 2nd GudB activity phase) that becomes longer as the complex concentration decreases. The inset shows the phase 3 in each of the individual progress curves. **(o)** Unlike phase 2, phase 3 that corresponds to GltAB's activity shows linear dependence with enzyme concentration. The inset shows phase 3 in each of the individual progress curves. Data in panels g-o are from single experiment and are representative of at least 2 independent experiments.

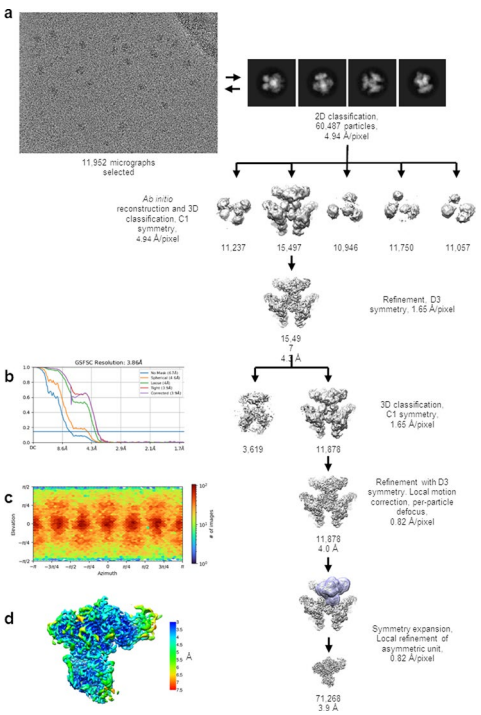

Extended Data Fig. 4 | Cyro-EM image processing for $GudB_6$-$GltA_6B_6$. (a) Scheme for single particle cryo-EM analysis of the $GudB_6$-$GltA_6B_6$. Details of the process are described in the Methods section. Briefly, particles were iteratively picked from selected micrographs using well resolved 2D class averages, followed by Ab initio 3D reconstruction and classification into five classes. The best resolved 3D class was refined with D3 symmetry imposed. In order to account for deviations from D3 symmetry, further refinement focused on single GudB-GltAB asymmetric units. The number of particles that are included in the maps are indicated, along with the estimated resolution where relevant. **(b)** FSC curves for the refined GudB-GltAB asymmetric map. **(c)** Angular distribution plot. **(d)** 3D map colored according to local resolution estimate.

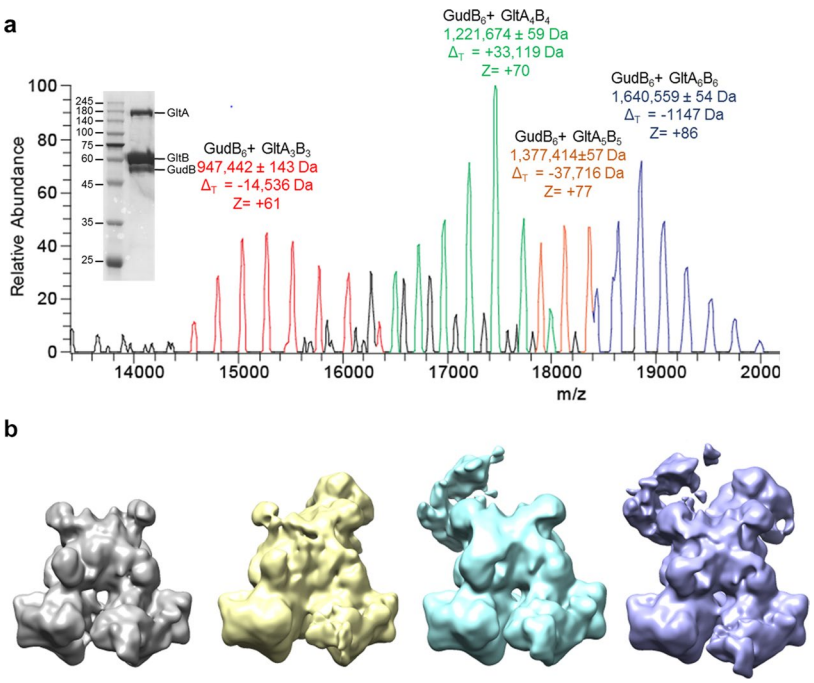

Extended Data Fig. 5 | Native-MS and the corresponding particle types observed in cryo-EM of the GudB enriched preparation of the GudB-GltAB complex. (a) Native-MS spectra showing different species of GudB-GltAB complex. These species primarily differ in the number of GltAB heterodimers attached to the GudB hexamer (from 3-6). Charge states (z) and the difference from theoretical mass (Δ_T) is indicated for each species. While the mass of the fully assembled complex agreed well with the expected mass, high Δ_T values of the other species could be because of degradation of some of the component proteins during the extended incubation step with *E. coli* lysate (Methods section) during the purification process. The inset shows the SDS-PAGE of GudB-GltAB complex used for the native-MS. The sample was prepared after enriching the *B. subtilis* lysate with recombinant GudB expressed and purified from *E. coli* (see Protein expression and purification, Methods). The image is from a single experiment and is a representative of at least two independent experiments. This sample contained a higher fraction of GudB and was also used for cryo-EM to obtain the high-resolution structure of $GudB_6$-$GltA_2B_2$ complex (Fig. 5). **(b)** Preliminary cryo-EM maps corresponding to different particle types ($GudB_6$-$GltA_{2\text{-}4}B_{2\text{-}4}$) observed. The key difference between particles is the number of GltAB subunits - the least being two (grey) and the maximum four (violet).

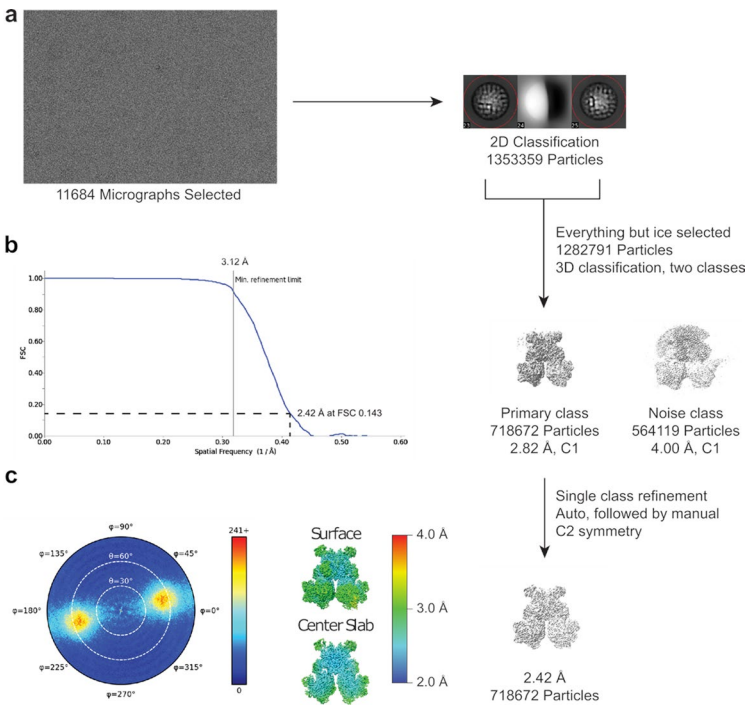

Extended Data Fig. 6 | Single particle cryo-EM analysis of the $GudB_6$-$GltA_2B_2$. (a) The particles were iteratively picked from selected micrographs and classified. All non-ice particles were carried forward and subjected to a two-class 3D auto refinement in cisTEM using the preliminary $GudB_6$-$GltA_2B_2$ reference. This yielded one noise class carrying unaligned particles and high frequency noise, and one class representing clear density for the $GudB_6$-$GltA_2B_2$ species. This class was refined using auto and manual methods in cisTEM, with C2 symmetry applied. The number of particles and the estimated resolution are indicated. **(b)** FSC curves for the refined $GudB_6$-$GltA_2B_2$ map. **(c)** Angular distribution plot and local resolution estimation (Relion3.1.2).

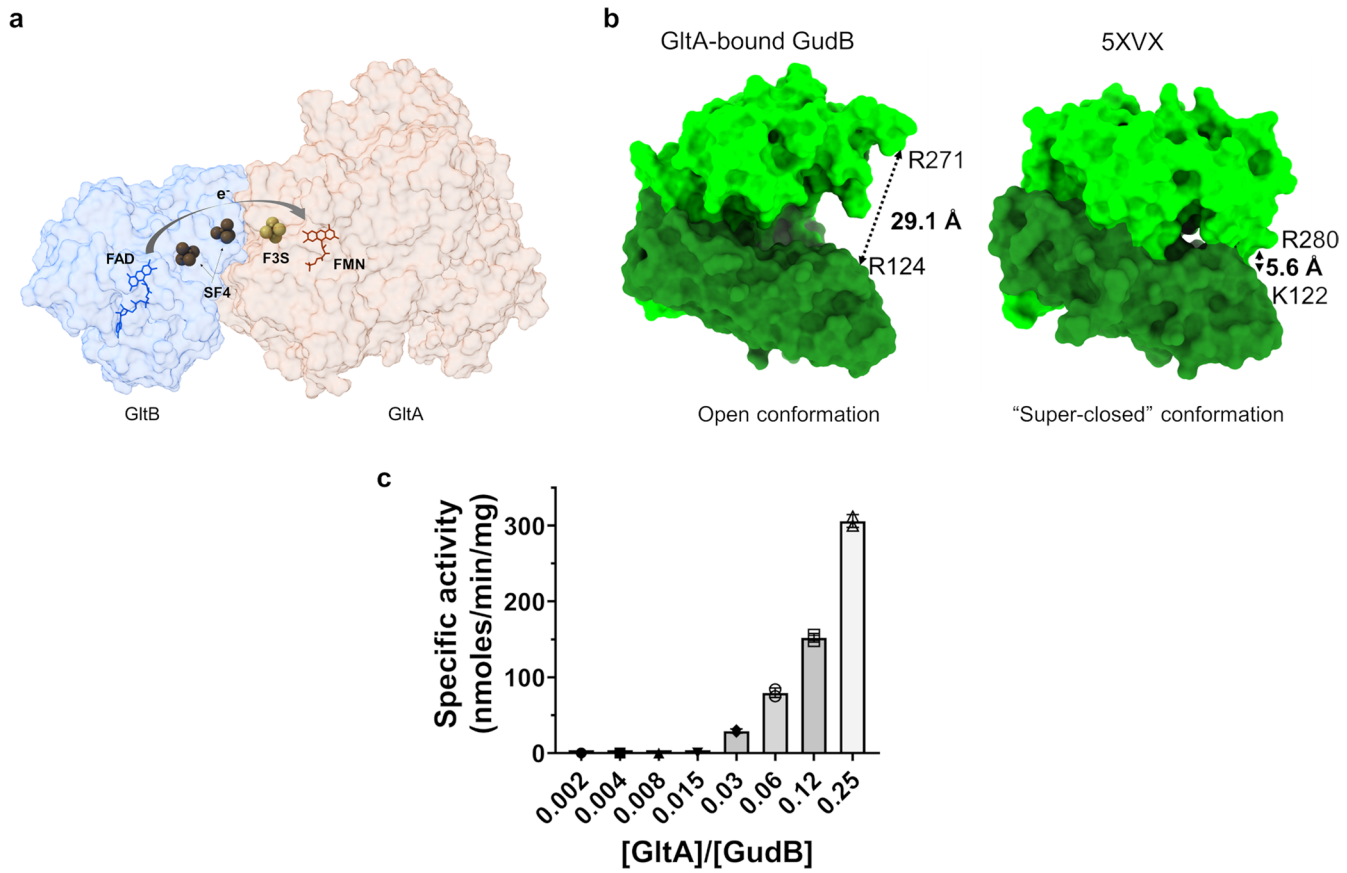

Extended Data Fig. 7 | Effect of GltA binding on GudB. (a) The co-factors in GltAB: FAD, two 4Fe-4S clusters (SF4), 3Fe-4S cluster (F3S) and FMN. These co-factors are involved in shuttling of electrons from NADPH to 2-iminoglutarate along shown arrow. GltA and GltB are shown in a transparent surface representation. **(b)** GltAB binding captures GudB in an 'open' state with the distance of 29.1 Å between residues R280 (in the co-factor binding domain, shown in light green) and K122 (in the substrate binding domain, shown in green). These residues are equivalent to R271 and R124 in the model of a 'super-closed' glutamate dehydrogenase (PDB 5XVX)[30] (right panel). **(c)** GltAB in sub-stoichiometric amounts promotes hexamerization of GudB by interacting with multiple GudB protomers (from different dimers, as shown in Fig. 5c) and hence prevents loss of activity. The assay buffer contained 400 mM glutamate and 4 mM NAD^+ and the reaction was initiated by the addition of an enzyme mix consisting of GudB pre-incubated with different amounts of GltAB (in all the reactions, GudB was present at a final concentration is 0.05 µM). GltAB prevents GudB inactivation in a concentration dependent manner. Individual data points are shown from two independent measurements and error bars indicate standard deviation of the mean.

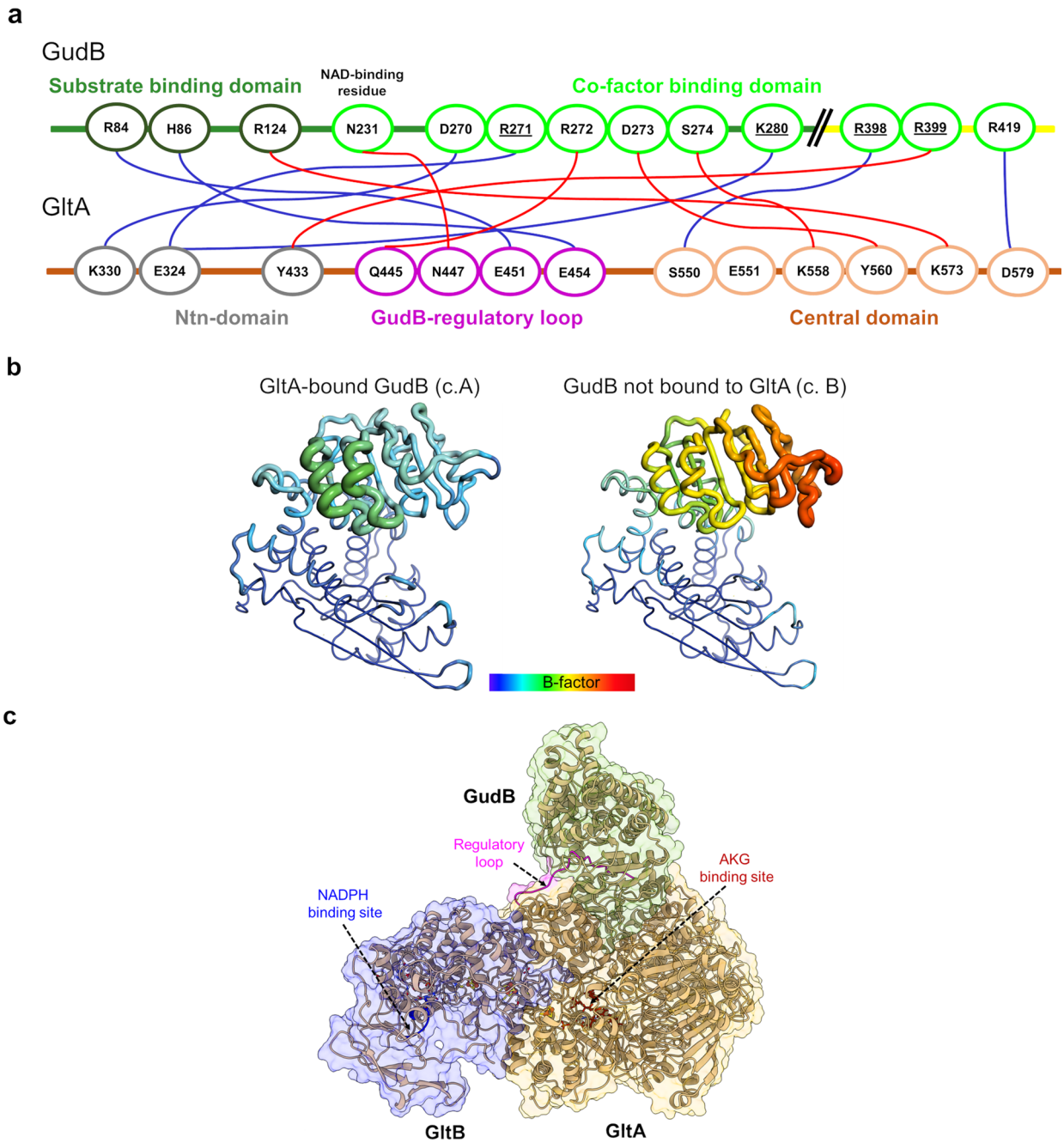

Extended Data Fig. 8 | Details of the GudB-GltAB interaction. (a) Key interactions between GltA (ovals on orange line) and two GudB protomers (ovals on green/major interaction and yellow line/minor interaction); salt bridges are shown in red and hydrogen bonds in blue. The border of ovals are colored based on domain/structural feature to which the residue belongs. **(b)** Binding to GltA stabilizes many loops in the cofactor binding domain of GudB. Shown are a GltA-bound GudB protomer (left, chain A in 7MFM) and a free GudB protomer in the same structure (right, chain B) in the 'putty' representation as implemented in PyMol. The radius of the ribbon increases from low to high B-factor and the Cα B-factors are shown in dark blue (lowest B-factor, 54) to red (highest B-factor, 163). nding site is located about 45 Å and 75 Å from the regulatory loop of GltA.

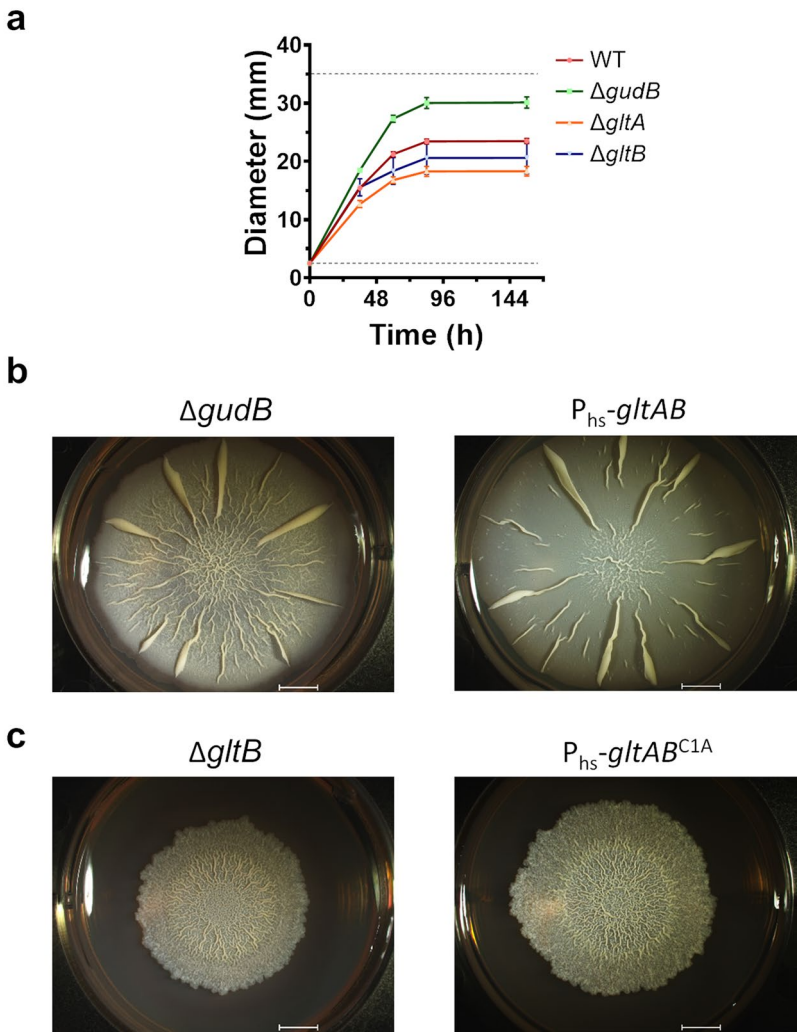

Extended Data Fig. 9 | Biofilm growth and disruption phenotypes. (a) Biofilm diameters measured at different time points. While Δ*gudB* biofilms were bigger in size and grew faster than wild-type biofilms, Δ*gltA* and Δ*gltB* biofilms were smaller. The dashed lines at 2.5 mm and 35 mm indicates the starting size of the biofilm, and the diameter of the well, used to grow the biofilm, respectively. The measurements were from four independent experiments (n = 4). Data is shown as mean and error bars represent standard deviation. **(b)** Similarity in biofilm morphology between Δ*gudB* and the P_{hs}-*gltAB* strains (grown with 100 μM IPTG). Overexpression of GltAB in the latter increases in synthase activity and also silences GudB, thereby resembling the Δ*gudB* biofilm morphology. Both biofilms grew rapidly and had large wrinkles spreading from the interior to the periphery of the biofilm. All the images in this panel are reproduced from Fig. 6 for better representation of the biofilm morphology. **(c)** Similarity in biofilm morphology between Δ*gltB* and the P_{hs}-*gltAB*^{C1A} strains (grown with 100 μM IPTG). In both the biofilms the wrinkles are restricted to the interior of the biofilm.

nature research

Corresponding author(s): Vijay Jayaraman, James S. Fraser

Last updated by author(s): Sep 13, 2021

Reporting Summary

Nature Research wishes to improve the reproducibility of the work that we publish. This form provides structure for consistency and transparency in reporting. For further information on Nature Research policies, see our Editorial Policies and the Editorial Policy Checklist.

Statistics

For all statistical analyses, confirm that the following items are present in the figure legend, table legend, main text, or Methods section.

n/a	Confirmed
☐	☒ The exact sample size (*n*) for each experimental group/condition, given as a discrete number and unit of measurement
☐	☒ A statement on whether measurements were taken from distinct samples or whether the same sample was measured repeatedly
☒	☐ The statistical test(s) used AND whether they are one- or two-sided *Only common tests should be described solely by name; describe more complex techniques in the Methods section.*
☒	☐ A description of all covariates tested
☒	☐ A description of any assumptions or corrections, such as tests of normality and adjustment for multiple comparisons
☐	☒ A full description of the statistical parameters including central tendency (e.g. means) or other basic estimates (e.g. regression coefficient) AND variation (e.g. standard deviation) or associated estimates of uncertainty (e.g. confidence intervals)
☒	☐ For null hypothesis testing, the test statistic (e.g. *F*, *t*, *r*) with confidence intervals, effect sizes, degrees of freedom and *P* value noted *Give P values as exact values whenever suitable.*
☒	☐ For Bayesian analysis, information on the choice of priors and Markov chain Monte Carlo settings
☒	☐ For hierarchical and complex designs, identification of the appropriate level for tests and full reporting of outcomes
☒	☐ Estimates of effect sizes (e.g. Cohen's *d*, Pearson's *r*), indicating how they were calculated

Our web collection on statistics for biologists contains articles on many of the points above.

Software and code

Policy information about availability of computer code

Data collection	Biotek Gen5 (bacterial growth and enzyme kinetics), Serial-EM (CryoEM data collection), MotionCor2
Data analysis	Pymol (2.4.1), Graph pad prism (9.2), CryoSPARC (3.1.0), cisTEM, ChimeraX (1.1.1), ISOLDE (1.1.0), coot (0.9.3), and PHENIX (1.19), Xcalibur (v4.1.31.9), Masslynx 4.2, MaxQuant v1.6.0.16, Perseus v1.6.0.7, DiscoverMP,

For manuscripts utilizing custom algorithms or software that are central to the research but not yet described in published literature, software must be made available to editors and reviewers. We strongly encourage code deposition in a community repository (e.g. GitHub). See the Nature Research guidelines for submitting code & software for further information.

Data

Policy information about availability of data

All manuscripts must include a data availability statement. This statement should provide the following information, where applicable:

- Accession codes, unique identifiers, or web links for publicly available datasets
- A list of figures that have associated raw data
- A description of any restrictions on data availability

The proteomics data is provided as excel sheet (Supplementary dataset 1 and 2). The structural data is deposited in the PDB (PDB code: 7MFM and 7MFT).

Field-specific reporting

Please select the one below that is the best fit for your research. If you are not sure, read the appropriate sections before making your selection.

☒ Life sciences ☐ Behavioural & social sciences ☐ Ecological, evolutionary & environmental sciences

For a reference copy of the document with all sections, see nature.com/documents/nr-reporting-summary-flat.pdf

Life sciences study design

All studies must disclose on these points even when the disclosure is negative.

Sample size	Sample size of n=3 was used for growth experiments and n=2 for in vitro kinetics experiments and n=4 for biofilm growth measurements.
Data exclusions	No data was excluded for the analysis
Replication	All the experiments involving growth profiling of strains and enzyme kinetics had at least two technical and biological replicates.
Randomization	This is not relevant to the study as the results are biochemical studies that are generally invariant to randomization
Blinding	Blinding is not relevant to the study as the study involves biochemical studies that yields objective data.

Reporting for specific materials, systems and methods

We require information from authors about some types of materials, experimental systems and methods used in many studies. Here, indicate whether each material, system or method listed is relevant to your study. If you are not sure if a list item applies to your research, read the appropriate section before selecting a response.

Materials & experimental systems

n/a	Involved in the study
☐	☒ Antibodies
☒	☐ Eukaryotic cell lines
☒	☐ Palaeontology and archaeology
☒	☐ Animals and other organisms
☒	☐ Human research participants
☒	☐ Clinical data
☒	☐ Dual use research of concern

Methods

n/a	Involved in the study
☒	☐ ChIP-seq
☒	☐ Flow cytometry
☒	☐ MRI-based neuroimaging

Antibodies

Antibodies used	anti-GudB antibody , HRP-conjugated anti-Rabbit IgG (Jackson ImmunoResearch,111-035-144)
Validation	Antibody was produced against recombinant Bacillus subtilis GudB expressed in E. coli. Antibodies were validated using western analysis on B. subtilis lysate.